Micron 151 (2021) 103141

Contents lists available at ScienceDirect

Micron

journal homepage: www.elsevier.com/locate/micron

Tutorial

Prismatic 2.0 – Simulation software for scanning and high resolution transmission electron microscopy (STEM and HRTEM)

Luis Rangel DaCosta [a,b,*], Hamish G. Brown [a], Philipp M. Pelz [a,b], Alexander Rakowski [a], Natolya Barber [a], Peter O'Donovan [c], Patrick McBean [c,d], Lewys Jones [c,d], Jim Ciston [a], M. C. Scott [a,b], Colin Ophus [a,*]

[a] National Center for Electron Microscopy, Molecular Foundry, Lawrence Berkeley National Laboratory, 1 Cyclotron Road, Berkeley, CA, USA
[b] Department of Materials Science and Engineering, University of California Berkeley, Berkeley, CA 94720, USA
[c] School of Physics, Trinity College Dublin, Dublin 2, Ireland
[d] Advanced Microscopy Laboratory, Centre for Research on Adaptive Nanostructures and Nanodevices (CRANN), Dublin 2, Ireland

ARTICLE INFO

Keywords:
Electron scattering
Transmission electron microscopy
Scanning transmission electron microscopy
Simulation
Open source

ABSTRACT

Scanning transmission electron microscopy (STEM), where a converged electron probe is scanned over a sample's surface and an imaging, diffraction, or spectroscopic signal is measured as a function of probe position, is an extremely powerful tool for materials characterization. The widespread adoption of hardware aberration correction, direct electron detectors, and computational imaging methods have made STEM one of the most important tools for atomic-resolution materials science. Many of these imaging methods rely on accurate imaging and diffraction simulations in order to interpret experimental results. However, STEM simulations have traditionally required large calculation times, as modeling the electron scattering requires a separate simulation for each of the typically millions of probe positions. We have created the `Prismatic` simulation code for fast simulation of STEM experiments with support for multi-CPU and multi-GPU (graphics processing unit) systems, using both the conventional multislice and our recently-introduced PRISM method. In this paper, we introduce `Prismatic` version 2.0, which adds many new algorithmic improvements, an updated graphical user interface (GUI), post-processing of simulation data, and additional operating modes such as plane-wave TEM. We review various aspects of the simulation methods and codes in detail and provide various simulation examples. `Prismatic` 2.0 is freely available both as an open-source package that can be run using a C++ or Python command line interface, or GUI, as well within a Docker container environment.

1. Introduction

Transmission electron microscopy (TEM) is heavily used in both materials science and biological studies of materials on the nanoscale, due to its high spatial resolution and the flexibility of operating modes (Egerton et al., 2005). TEM experiments can be performed using plane wave illumination, where users can either record the far field intensity as a diffraction pattern (Williams et al., 2009) or by forming an image of the electron wave after it has been transmitted through the sample, often referred to as high-resolution transmission electron microscopy (HRTEM) (Buseck et al., 1989). Alternatively, the electron beam can be focused into a small spot and scanned over the sample surface, which is referred to as scanning transmission electron microscopy (STEM) (Pennycook and Nellist, 2011). The introduction of spherical aberration correctors in the past few decades enable the formation of a finer probe in STEM (Batson et al., 2002) and point-spread function in HRTEM (Haider et al., 1998). Aberration-corrected TEM and STEM have greatly facilitated many atomic resolution experiments, including imaging single-layer graphene sheets (Gass et al., 2008; Robertson and Warner, 2013), elemental mapping (Kothleitner et al., 2014), atomic electron tomography (Yang et al., 2017), vibrational spectroscopy (Venkatraman et al., 2019), observation of polar skyrmions (Das et al., 2019), and many others.

With the widespread adoption of charge-coupled device cameras (Krivanek and Mooney, 1993), and later direct electron detectors (MacLaren et al., 2020), both STEM and TEM are now fully digital sciences. Augmenting STEM and TEM experiments with modern data science methods holds enormous promise for future experimentation

* Corresponding authors.
E-mail addresses: luisrd@berkeley.edu (L. Rangel DaCosta), cophus@gmail.com (C. Ophus).

https://doi.org/10.1016/j.micron.2021.103141
Received 31 May 2021; Received in revised form 20 August 2021; Accepted 22 August 2021
Available online 10 September 2021

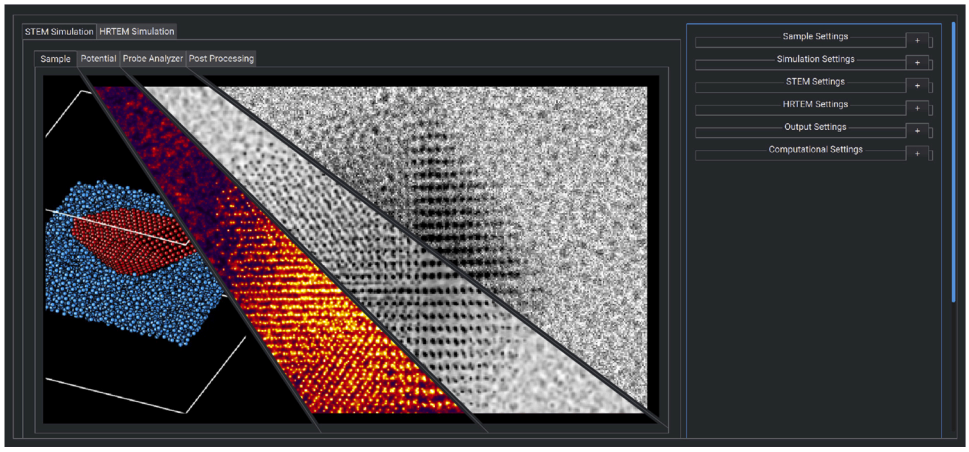

Fig. 1. Updated `Prismatic` 2.0 GUI. Previews of interactive tabs are shown in center panel.

(Spurgeon et al., 2020). One of the most data-intensive families of STEM experiments is the use of fast direct electron detectors to collect thousands or even millions of 2D images of the diffracted probes over a 2D grid of probe positions, often referred to as a four dimensional-STEM (4D-STEM) dataset (Ophus, 2019). One of the key ingredients for developing and implementing new computational methods is the ability to perform forward simulations of the various STEM and TEM experimental methods (LeBeau et al., 2008; Zhang et al., 2020). HRTEM simulations and STEM simulations for the 2D, 3D, or 4D experiments described above are typically performed using the multislice method (Cowley and Moodie, 1957; Kazuo and Natsu, 1977). However, these simulations have traditionally required very long compute times, due to the fact that a separate multislice simulation must be performed for each new probe position (Kirkland, 2020).

In a previous study, Ophus (2017) introduced a new algorithm, named plane-wave reciprocal-space interpolated scattering matrix (PRISM) for simulation of STEM experiments. The PRISM algorithm involves calculating and storing a compact scattering matrix operator which can be rapidly applied to each of the probe wavefunctions to model their propagation through the sample. This algorithm can potentially increase the speed of STEM image simulations by multiple orders of magnitude. The PRISM algorithm was first implemented into the original `Prismatic` simulation code by Pryor et al. (2017). Since then, PRISM has been adapted for double-channeling STEM-EELS simulation by Brown et al. (2019); it has been separately implemented for image simulation by Brown et al. (2020) and Madsen and Susi (2021).

`Prismatic` is intended for use as a fully-featured TEM/STEM simulation software for electron microscopy, for diverse use cases such as experimental validation, database generation, or teaching. It also serves as the reference implementation for the aforementioned PRISM algorithm. `Prismatic` is an open-source and cross-platform software package that can be easily installed, easily used, and that comes with a GUI. The software is primarily written in C++ with CUDA modules for GPU acceleration to take advantage of available computing and HPC resources and is readily integrated into other scientific open-source software for microscopy applications such as py4DSTEM (Savitzky et al., 2021).

In this paper, we present `Prismatic` version 2.0, a software package for image and diffraction space simulations of electron scattering for both STEM and HRTEM. `Prismatic` v2.0 has many new basic features, such as performing HRTEM simulations, increased support for arbitrary aberrations, support for arbitrary STEM scan patterns, focal series simulations, and enhanced support for generalized input and output. We have also added several improvements to enhance the accuracy and speed of simulations, including a new approach for the correct subslicing of 3D atomic potentials with sub-pixel shifting, a refocusing approach to the scattering matrix calculation for PRISM simulations that increases accuracy for thicker samples and delocalized probes, and various post-processing methods for coherence or shot-noise limitations. We have added many upgrades to the code, including new pipelines for compiling, a unit-testing suite, an overhauled GUI system (previewed in Fig. 1), and pre-compiled Docker containers for ready-to-use installations of the command-line and `pyprismatic` interfaces. In this paper, we explain these methods and additions in detail, as well as demonstrate several new applications for `Prismatic` and some uses of the Python bindings in `pyprismatic`.

2. Theory

2.1. The multislice method

We describe the electron beam using a complex wavefunction $\psi(x, y, z)$, where $\langle x, y, z\rangle$ are the real space coordinate system. When considering only forward scattering, we can reduce the problem to the evolution of a 2D wavefunction $\psi(\mathbf{r})$ along the optical axis z, where $\mathbf{r} = \langle x, y\rangle$. This evolution is described by the paraxial Schrödinger equation for fast electrons (Van Dyck, 1985)

$$\frac{\partial\psi(\mathrm{r})}{\partial z} = \frac{i\lambda}{4\pi}\nabla^2\psi(\mathrm{r}) + i\sigma V(\mathrm{r})\psi(\mathrm{r}), \tag{1}$$

where i is the imaginary constant and $V(\mathbf{r})$ is the electrostatic potential, usually corresponding to the sample. The relativistically-corrected electron-matter interaction constant σ is given by

$$\sigma = \frac{2\pi\gamma m_e q_e \lambda}{h^2}, \tag{2}$$

where γ, m_e, q_e, λ, and h are the relativistic correction factor, the electron mass, the electron charge, the relativistically corrected electron wavelength, and the Planck constant respectively.

The two operators on the right-hand side of Eq. (1) do not commute so a widely utilized numerical approach to its solution is a split-step method first derived by Cowley and Moodie (1957). For small changes in z, Eq. (1) can be solved in two steps, taking first only the ∇^2 term and then the V term into account. First, we divide up the sample into a series of N slices, $V_n(\mathbf{r})$, which are 2D arrays that integrate the electrostatic potential contained in a given slice of thickness Δz, given by

$$V_n(\mathrm{r}) = \int_{z-\Delta z/2}^{z+\Delta z/2} V(\mathrm{r})\mathrm{d}z. \tag{3}$$

The solution to Eq. (1) taking into consideration just V on the right-hand side is

$$\psi(\mathrm{r}) = T(\mathrm{r})\psi_0(\mathrm{r}) = e^{i\sigma V_n(\mathrm{r})}\psi_0(\mathrm{r}), \tag{4}$$

where $\psi_0(\mathbf{r})$ is the input wavefunction and $T(\mathbf{r})$ is referred to as the transmission function. This is equivalent to the so-called "phase object" approximation which holds for samples thin enough to ignore the effects of thickness. For the next part of the split-step solution, where we assume $V_n(\mathbf{r}) = 0$, the operator ∇^2 can be efficiently applied in Fourier space (Kazuo and Natsu, 1977; Kirkland, 2020), giving

$$\psi(\mathrm{r}) = \widehat{\mathcal{F}}^{-1}_{\mathrm{k}\to\mathrm{r}}\left\{e^{i\lambda\Delta z|\mathrm{k}|^2}\widehat{\mathcal{F}}_{\mathrm{r}\to\mathrm{k}}[\psi_0(\mathrm{r})]\right\} \tag{5}$$

The term $e^{i\lambda\Delta z|\mathrm{k}|^2}$, referred to as the propagation operator, uses the 2D reciprocal space coordinates $\mathbf{k} = (k_x, k_y)$, and the forward and inverse 2D Fourier transform operations denoted by $\widehat{\mathcal{F}}_{\mathrm{r}\to\mathrm{k}}$ and $\widehat{\mathcal{F}}^{-1}_{\mathrm{k}\to\mathrm{r}}$ respectively. Eqs. (4) and (5) are alternately applied to calculate the final wavefunction after interacting with the sample,

$$\psi(\mathrm{r}) = \prod_{n=1}^{N}\{\widehat{\mathcal{F}}^{-1}_{\mathrm{k}\to\mathrm{r}}[e^{i\lambda\Delta z|\mathrm{k}|^2}\{\widehat{\mathcal{F}}_{\mathrm{r}\to\mathrm{k}}[e^{i\sigma V_n(\mathrm{r})}]\}]\}\psi_0(\mathrm{r}), \tag{6}$$

which is typically referred to as the exit wave. This numerical solution is called the "multislice method" (Cowley and Moodie, 1957). It requires N transmission operations and $N-1$ propagation operations, and is the most common simulation algorithm for modeling TEM experiments (Kirkland, 2020).

Alternatively the operator-product in Eq. (6) can be encapsulated as single matrix equation (Sturkey, 1962)

$$\psi(\mathrm{r}) = \mathcal{S}_{\mathrm{r,k}}\widehat{\psi}_0(\mathrm{k}), \tag{7}$$

where we have opted to start with the probe in reciprocal space on the right hand side with the exit-surface wave function on the left hand side being in real space. The concept of the scattering matrix is common in quantum mechanics for calculating scattering behavior of electrons and other charged particles (Weinberg, 1995) and is typically purely in reciprocal space. For our purposes it will be more convenient to use the reciprocal space to real space formulation in Eq. (7) since the STEM probe is compact in reciprocal space and the PRISM algorithm will involve cropping the exit wave in real space. The rows or columns of $\mathcal{S}$ can be changed from real to reciprocal space or vice versa with the operation of the appropriate $\widehat{\mathcal{F}}_{\mathrm{r}\to\mathrm{k}}$ or $\widehat{\mathcal{F}}^{-1}_{\mathrm{k}\to\mathrm{r}}$ applied either to the left or right side of $\mathcal{S}$.

2.2. Calculation of projected potentials

The calculation of the atomic scattering potential $V_n(\mathbf{r})$ is one of the most crucial aspects of scattering simulations. The discretization of the scattering potential limits the accuracy and total amount of information that can be transmitted and propagated; any artifacts created in the calculation of $V_n(\mathbf{r})$ can lead to nonphysical behavior in the elastic scattering calculations. Many implementations of the scattering potential utilize the isolated atom approach, where the total potential is the sum of potentials of independent, isolated atoms such that

$$V_n(r) = \sum V_i(r) \tag{8}$$

where i is the index of each atom. The isolated atom approach, since each atom of a given species is independent and equivalent, can take advantage of a precomputed look-up table. Generally, this approach is computationally cheap and simple to implement, and correctly accounts for the dominant aspect of nuclear scattering but inherently does not capture bonding effects. Analytical scattering potentials do not exist for elements other than hydrogen; the rest of the atomic species are typically parameterized based on single atom scattering factors determined through Hartree–Fock calculations, like in the parameterization by Kirkland (2020)

$$\begin{aligned} V(\mathrm{r}) = \quad & 2\pi^2 a_0 q_e \sum_i \frac{a_i}{\mathrm{r}} exp(-2\pi\mathrm{r}\sqrt{b_i}) \\ & +2\pi^{5/2} a_0 q_e \sum_i c_i d_i^{-3/2} exp(-\pi^2\mathrm{r}^2 \Big/ d_i) \end{aligned} \tag{9}$$

where a_0 is the Bohr radius and a_i, b_i, c_i, and d_i are fitted parameters. This parameterization can also be integrated analytically along the beam direction so that the contribution of an atom to its two-dimensional slice can be calculated directly

$$\begin{aligned} V_z(\mathrm{r}) = \quad & 4\pi^2 a_0 e \sum_i a_i K_0(2\pi\mathrm{r}\sqrt{b_i}) \\ & +2\pi^2 a_0 e \sum_i \frac{c_i}{d_i} exp(-\pi^2\mathrm{r}^2 \Big/ d_i) \end{aligned} \tag{10}$$

where K_0 is the modified Bessel function.

However, 2D scattering potential calculations cannot perfectly capture the 3D scattering of real atoms, since atoms must first be assigned to discrete projected potential slices before integration – an explicitly 3D integration of the potential into the different potential slices can more accurately capture this 3D scattering (Lobato and Van Dyck, 2015). Simple isolated atom implementations are also often pixel-limited in the planar directions, such that the atomic center can only exist on discrete pixels. This can fail to capture the subtlety of the real positions of atoms, especially when considering thermal vibration effects. Sub-pixel accuracy, however, can be costly to implement and hard to achieve. One possible strategy is to forgo the use of a look-up table and instead integrate each atom directly on sub-pixel grids, which can become prohibitive for especially large cells. Alternatively, one could apply some sort of sub-pixel shift in the transverse direction, which can introduce artifacts into the scattering potential if implemented poorly. Alternative 3D integration methods for computing atomic potentials have been given by Lobato and Van Dyck (2015) and Madsen and Susi (2021). Atomic potentials can also be directly evaluated electron densities as calculated using Density Functional Theory calculations, as by Madsen and Susi (2021).

2.3. The plane-wave reciprocal-space interpolated scattering-matrix (PRISM) algorithm for STEM simulation

In a conventional multislice simulation, each STEM probe position requires independent evaluation of the propagation through the potential as described by Eqs. (5) and (6). Introduced in Ophus et al. (2016a) and implemented in Pryor et al. (2017), Brown et al. (2020), Madsen and Susi (2021), the PRISM algorithm is a STEM simulation technique for which scaling of the compute time with the number of probe positions is generally more favorable. In PRISM, instead of directly forming the incident probe wavefunction and propagating the wavefunction through the projected potential via the multislice algorithm, we instead calculate and store the $\mathcal{S}$-matrix in Eq. (7) for a basis set of incident plane waves. The $\mathcal{S}$-matrix can be reused for any number of STEM probes once it has been calculated, and thus, we can trade the upfront computation of S for the much greater acceleration in the output calculation stage. Further speed ups for a modest loss of simulation accuracy can be achieved through coarsening of the input plane-wave basis (by only calculating every f^{th} plane wave from the original simulation grid; f is known as the PRISM interpolation factor) and reciprocal-space interpolation of the output wave function (achieved by real-space cropping of the output wave to a square region measuring $1/f$ of the simulation grid). The reciprocal-space interpolation grants the user a large amount of control of the speed and accuracy of the simulation, which could otherwise only be done in the multislice algorithm

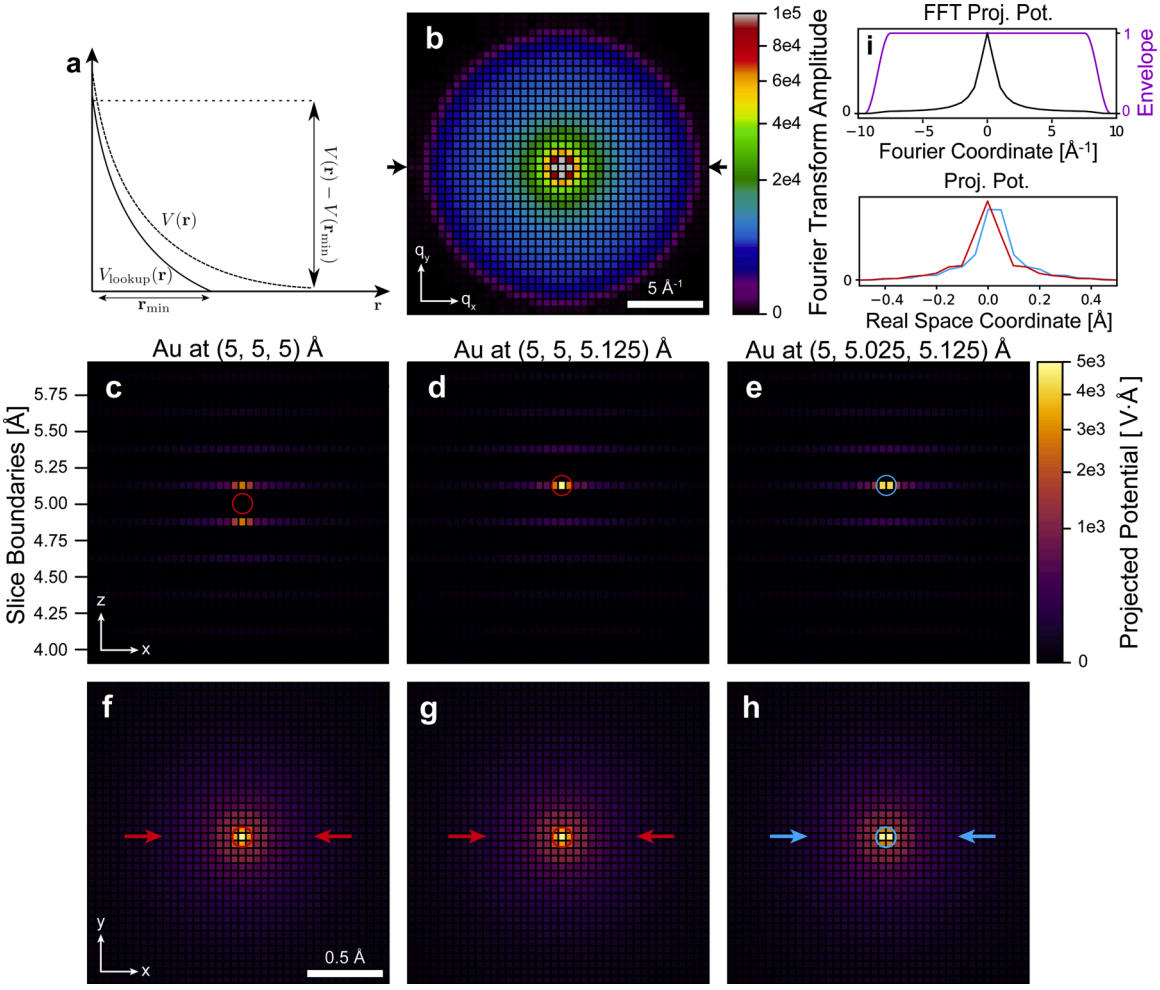

Fig. 2. 3D projected potential calculation. (a) Lookup tables $V_{\text{lookup}}(\mathbf{r})$ of the potential for each atom are calculated out to some radius $\mathbf{r}_{\text{min}}$. The potential at this radius $V(\mathbf{r}_{\text{min}})$ subtracted so as to remove the abrupt step that would otherwise result at $\mathbf{r}_{\text{min}}$ when the potential was placed on the larger array. (b) Representative Fourier transform amplitude of atoms shown in (f)–(h). A slice of the x–z plane of the 3D projected potentials of a single Au atom (c) shifted one half slice along the z direction, (d) shifted one half pixel along the z direction, and (e) shifted one half pixel along both x and z directions. Circles represent position of atom. (f)–(h) Total projected potential of single Au atoms, corresponding to (c)–(e) respectively. (i) Line trace (top) taken from (b), showing the envelope function $B(\mathbf{k})$ applied in Fourier space to dampen the large scattering angles and line traces of real space potentials (f)/(g) (red) and (h) (blue). v All images have square root intensity scaling to highlight the weakly scattering regions.

by tuning the resolution of the projected potential or resampling of the diffraction patterns. For a more in-depth discussion of the PRISM algorithm, we refer readers to Ophus et al. (2016a), or the recent updates to PRISM given by Brown et al. (2019) and Pelz et al. (2021).

3. Methods

3.1. Numerical calculation of 3D potentials

We address the issues sometimes encountered with projection of the atomic potentials into single 2D slices by implementing 3D potential integration with sub-pixel accuracy of the atomic positions by use of a pre-calculated look-up table, which is sampled more finely than the multislice slice sampling in the propagation direction, alongside sub-pixel accuracy Fourier shifting of the potentials in the plane perpendicular to propagation. Our implementation is designed to improve upon simple 2D integration in a manner that is robust in various simulation conditions, is easy to understand and tune, and does not sacrifice a significant amount of computation. We first calculate the atomic potential for each unique species in the system on a local pixel grid $\mathbf{R} = (x_r, y_r, z_r)$, using the three-dimensional parameterization described in Eq. (9), where x_r, y_r are coordinates in the plane perpendicular to propagation and at the same resolution as the final potential field, and z_r is the coordinate along the propagation axis at some integer subsampling N_z of the final slice thickness t. Eq. (9) is evaluated out to maximum radius r_{max}, which along with the real space potential samplings r_x, r_y, and t/N_z determine the dimensions of the grid $\mathbf{R}$. The minimal coordinate of the atomic potential is $\mathbf{R} = (r_x, r_y, 0)$ which avoids the discontinuity otherwise present at $\mathbf{R} = 0$. To prevent sharp steps in the potential at the extremities of r_{max}, we subtract the value of $V(\mathbf{r})$ at the smallest extent of the atom in any of x_r, y_r, and z_r and then clamp any negative values to zero such that

$$V_{\text{lookup}}(\mathrm{r}) = max[V(\mathrm{r}) - V(\mathrm{r}_{\text{min}}),\ \ 0.0], \tag{11}$$

where

$$\mathbf{r}_{\text{min}} = \min\left[\max\left(x_r\right), \max\left(y_r\right), \max\left(z_r\right)\right] \tag{12}$$

This procedure is sketched in Fig. 2(a). The potential for each unique species is then stored in a look-up table after a 2D Fourier transform in x and y such that

$$V_{\text{lookup}}(\mathrm{k}, z) = \widehat{\mathcal{F}}_{\mathrm{r}\to\mathrm{k}}\{V_{\text{lookup}}(\mathrm{r})\} \tag{13}$$

since the subpixel shifts will be applied in Fourier space.

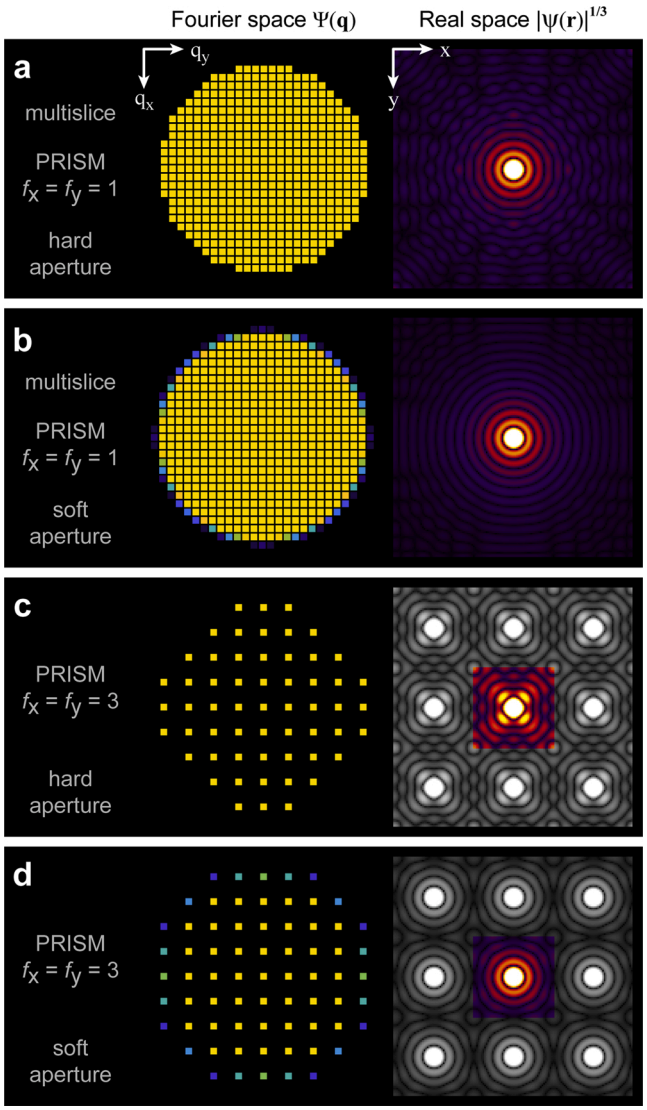

Fig. 3. Comparison of hard-aperture and soft-aperture STEM probes. Initial STEM probe defined with (a) a hard aperture edge, and (b) a soft aperture edge. Initial STEM probes for PRISM with $f_x = f_y = 3$, for (c) a hard aperture edge, and (d) a soft aperture edge. The soft edge minimizes artifacts resulting from the periodic boundary conditions inherent in all STEM simulations, PRISM simulations are colored inside the cropping box in real space.

To achieve sub-pixel positioning of the ith atom, to position (x_i, y_i), in the plane perpendicular to the beam propagation direction we apply a Fourier shift to the transformed potential $V(\mathbf{k}, z)$ based on the difference between the rounded pixel position of the atom round(x_i/x_y) and its ideal fractional x_i/r_x position

$$V_{i,\text{shifted}}(\mathrm{k}, z) = V(\mathrm{k}, z) \cdot B(\mathrm{k}) \cdot exp(-2\pi i \mathrm{k} \cdot \mathrm{r}_{\text{shift}}) \tag{14}$$

where

$$\mathrm{r}_{\text{shift}} = [x_i/r_x - \text{round}(x_i/r_x), y_i/r_y - \text{round}(y_i/r_y)],$$

$B(\mathbf{k})$ is a soft bandwidth limit given by

$$B(\mathrm{k}) = sin^2\left\{\frac{\pi}{2} min\left[max\left(\frac{0.95 - 2|\mathrm{k}|/k_{\max}}{0.95 - 0.75}, 0.0\right), 1.0\right]\right\}$$

applied to the potential in reciprocal space, and $k_{\max}$ is the maximum reciprocal space coordinate of the grid on which the lookup tables is constructed. Application of the bandwidth limit $B(\mathbf{k})$ limits oscillations in real space. This applied shift moves the atom to the correct place in real space without creating significant artifacts in the potential in Fourier space (where the propagation calculation occurs) below the Nyquist limit. We note that a coarse real space sampling (i.e., large values for r_x and r_y) can inject oscillations into the tails of the potential. This can result in unphysical negative values of the scattering potential in real space. $V_{\text{shifted}}(\mathbf{k}, z)$ is then Fourier transformed back to real space upon which it is again bandlimited such that

$$V_i(\mathrm{r}) = \mathcal{F}_{\mathrm{q}\to\mathrm{r}}\{V_{i,\text{shifted}}(\mathrm{k}, z)\} \cdot \mathrm{r}_{\text{band}} \tag{15}$$

where

$$\mathrm{r}_{\text{band}} = \begin{cases} 1.0, & \left(\frac{x_r}{max(x_r)}\right)^2 + \left(\frac{y_r}{max(y_r)}\right)^2 \leq 1.0 \\ 0.0, & \text{otherwise} \end{cases} \tag{16}$$

This final potential is then added into the final cell array. Along the propagation direction, the superresolution z values of $V(r)$ are simply binned to their closest rounding slice. We found that interpolation of the potential along the propagation direction caused little to no increase in accuracy at the expense of artifact introduction, and thus, was not implemented.

3.2. STEM probe formation

The most common probe configuration for STEM experiments is given by a circular aperture in the condenser plane. The use of fast Fourier transforms (FFTs) to implement the multislice solution to Eq. (1) and to set up STEM probes enforces periodic boundary conditions which results in interference artifacts as the tails of the STEM probe approach the edges of the simulation grid. We find that implementing these STEM probes in `Prismatic` by using a soft aperture minimizes these artifacts. Fig. 3 shows a comparison between STEM probes defined using hard and soft aperture edges. A hard aperture probe is defined by the function

$$\Psi_0(\mathrm{k}) = \begin{cases} 1 & \text{if } |\mathrm{k}| \leq k_{\text{probe}} \\ 0 & \text{if } |\mathrm{k}| > k_{\text{probe}}, \end{cases} \tag{17}$$

where k_{probe} defines the maximum scattering vector included in the STEM probe, and is proportional to the maximum scattering angle α_{probe} by the expression $\alpha_{\text{probe}} = \lambda k_{\text{probe}}$. The soft aperture probe used in `Prismatic` is defined by

$$\begin{aligned} \Psi_0(\mathrm{k}) &= \min\left[\max\left(\frac{k_{\text{probe}}|\mathrm{k}| - |\mathrm{k}|^2}{||\mathrm{k} \odot \Delta\mathrm{k}||_2} + \frac{1}{2}, 0\right), 1\right], \\ \Psi_0(0) &= 1, \end{aligned} \tag{18}$$

where $\Delta\mathbf{k}$ are the 2D pixel sizes in Fourier space, $\odot$ is the Hadamard (element-wise) product, and $||\cdot||_2$ is the 2-norm. The term in the denominator of Eq. (18) is equal to the Fourier space pixel size $\Delta\mathbf{k}$ multiplied by the Fourier space coordinate $\mathbf{k}$, which depends on the local orientation of $\mathbf{k}$ if the two pixel sizes are not equal. If these two pixel sizes are equal (typical of square simulation cells), Eq. (18) reduces to

$$\Psi_0(\mathrm{k}) = \min\left[\max\left(\frac{k_{\text{probe}} - |\mathrm{k}|}{\Delta\mathrm{k}} + \frac{1}{2}, 0\right), 1\right]$$

Fig. 3(a) and (b) show an example using hard and soft apertures respectively for a multislice simulation, or a full size PRISM simulation. These cases are fairly similar, though the rings corresponding to the probe tails become inaccurate after the third ring due to interference with probe tails on the opposite side of the grid resulting from the inherent periodic boundary conditions.

In most cases this refinement will make only a minor improvement to simulation accuracy, but for smaller simulation cells in multislice, or smaller cropping boxes in PRISM simulations, using the correct aperture

becomes more important. Fig. 3c and d show hard and soft apertures respectively for a PRISM $f = 3$ simulation. In the real space image of the STEM probe, the regions outside of the cropping box are shown in a grey color scale. The soft aperture produces two accurate probe tail rings, while the hard aperture is inaccurate for all probe tails. The hard aperture in Fig. 3c even produces an asymmetric center lobe of the STEM probe. These examples are at a deliberately lower resolution and smaller grid real-space size than for a typical STEM simulation to more clearly demonstrate the importance of using an accurate soft aperture function for defining the initial STEM probes. To our knowledge, this is a novel feature in `Prismatic`.

3.3. Anti-aliasing of the transmission and propagation operators

As both the multislice and PRISM algorithms rely on propagation through the calculation of successive discrete FFTs, we must prepare arrays and calculations in a way that prevents aliasing artifacts. Aliasing artifacts arise when signals of different frequencies become indistinguishable from each other due to the discrete sampling of the signals. To prevent aliasing of the propagation wave function Ψ, we multiply the array with a binary anti-aliasing mask which removes pixels above the Nyquist limit (1/2 the extent of the array) from the calculation at each propagation and transmission step. This method causes an intensity loss of the parts of the wave-function that are scattered to high angles due to the anti-aliasing aperture, and may cause some inaccuracies in electrons that might multiply-scatter back into low angles. Applying an anti-aliasing filter at the Nyquist limit completely prevents highly scattered electrons from "wrapping around" the wavefunction and scattering through the periodic boundary. An alternative approach for anti-aliasing is to apply anti-aliasing filters to both the propagated wave function and the projected potential slices at 2/3rds the extent of the arrays (Kirkland, 2020; Lobato and Van Dyck, 2015). We note for clarity that in our implementation, the projected potential is not band-limited. One should set the real space sampling of the simulation such that the error converges in the scattered regions of interest such that the application of the anti-aliasing aperture does not affect the interpretation of the simulation results.

3.4. HRTEM simulations

TEM simulation can be performed using the exact same methods as STEM multislice by replacing the incident wave function with a plane wave, i.e.,

$$\Psi_0(\mathrm{k}) = \begin{cases} 1 & \text{if } \mathrm{k} = \mathrm{k}_{\mathrm{tilt}} \\ 0 & \text{otherwise} \end{cases}$$

where $\mathbf{k}_{\mathrm{tilt}}$ is the tilt of the beam. Since the *S*-matrix calculation in the PRISM method forms the transmitted STEM probe using a scattered plane-wave basis set, the implementation can be readily used for HRTEM simulations. In `Prismatic`, HRTEM simulations are now implemented through utilization of the *S*-matrix infrastructure, with added functionality for more granular control of the beam selection for propagating sets of plane waves simultaneously with the multislice algorithm. Specific tilt ranges and selections can be controlled both through radial and rectangular mask generation, and through use of the PRISM interpolation factor (which coarsens the grid of tilts available), for example, to test different beam tilts or to model angular coherence. HRTEM simulations in `Prismatic` are focused to the middle of the sample cell instead of the entrance surface as implicitly done for STEM simulations. In simulation, this is accomplished through application of a defocus propagator to each beam in the *S*-matrix after its standard calculation. The final output is formally the 3D complex-valued *S*-matrix, with unique plane wave tilts along the beam direction, which can be saved either as the complex wavefunction or as integrated intensities.

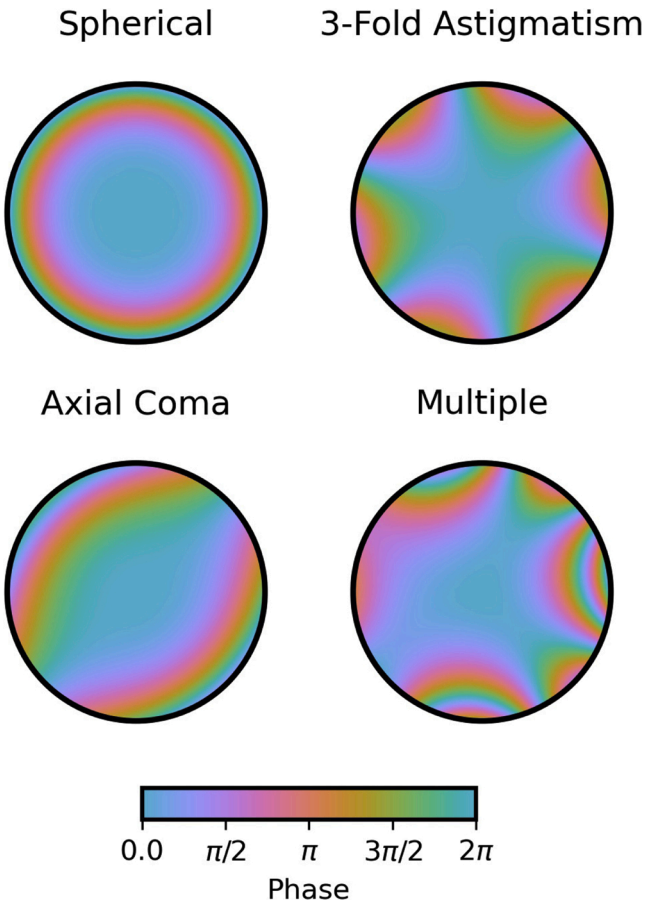

Fig. 4. Example aberration phase plates. From top-left to bottom-right, spherical aberration, 3-fold astigmatism, axial coma, and an arbitrary mixture of aberrations at 300 kV. Borders represent a cutoff of 2 inverse angstroms.

3.5. Aberrations

Coherent aberrations of the probe-forming lens in STEM and the image-forming lens in HRTEM simulations can be modeled through the inclusion of an aberration function χ when calculating the wave function in Fourier space such that

$$\Psi(k_x, k_y) = \Psi_0(k_x, k_y) exp[-i\chi(k_x, k_y)] \tag{19}$$

where Ψ_0 is the unaberrated wavefunction. χ can be expressed through a variety of appropriate basis sets (Krivanek, 1994; Thust et al., 1996; Uhlemann and Haider, 1998); in `Prismatic`, which now includes functionality to apply arbitrary sets of aberrations, we employ a unitless basis set similar to the one described in Ophus et al. (2016b). For aberrations with radial order m and azimuthal order n, the aberration function $\chi(\overrightarrow{k})$ can be fully described for coherent aberrations as

$$\begin{aligned} \chi(k_x, k_y) = &\sum_m \sum_n (\lambda \cdot |\mathrm{k}|)^m \cdot C_{m,n}^{\mathrm{mag}} \\ &\cdot \{cos[n \cdot C_{m,n}^{\mathrm{ang}}] \cdot cos[n \cdot \mathrm{atan2}(k_x, k_y)] \\ &+ sin[n \cdot C_{m,n}^{\mathrm{ang}}] \cdot sin[n \cdot \mathrm{atan2}(k_x, k_y)]\}, \end{aligned} \tag{20}$$

where λ is the electron wavelength, $C_{m,n}^{\mathrm{mag}}$ and $C_{m,n}^{\mathrm{ang}}$ are dimensionless coefficients describing the aberration magnitude in rads and azimuthal phase of an aberration, and atan2 is the 2-argument arctangent function which returns the polar angle of (k_x, k_y) in the correct quadrant. The dimensionless aberration coefficients are related to the convention in Ref. (Kirkland, 2011) which have units of length by $C_{m,n}^{\mathrm{mag}} =$

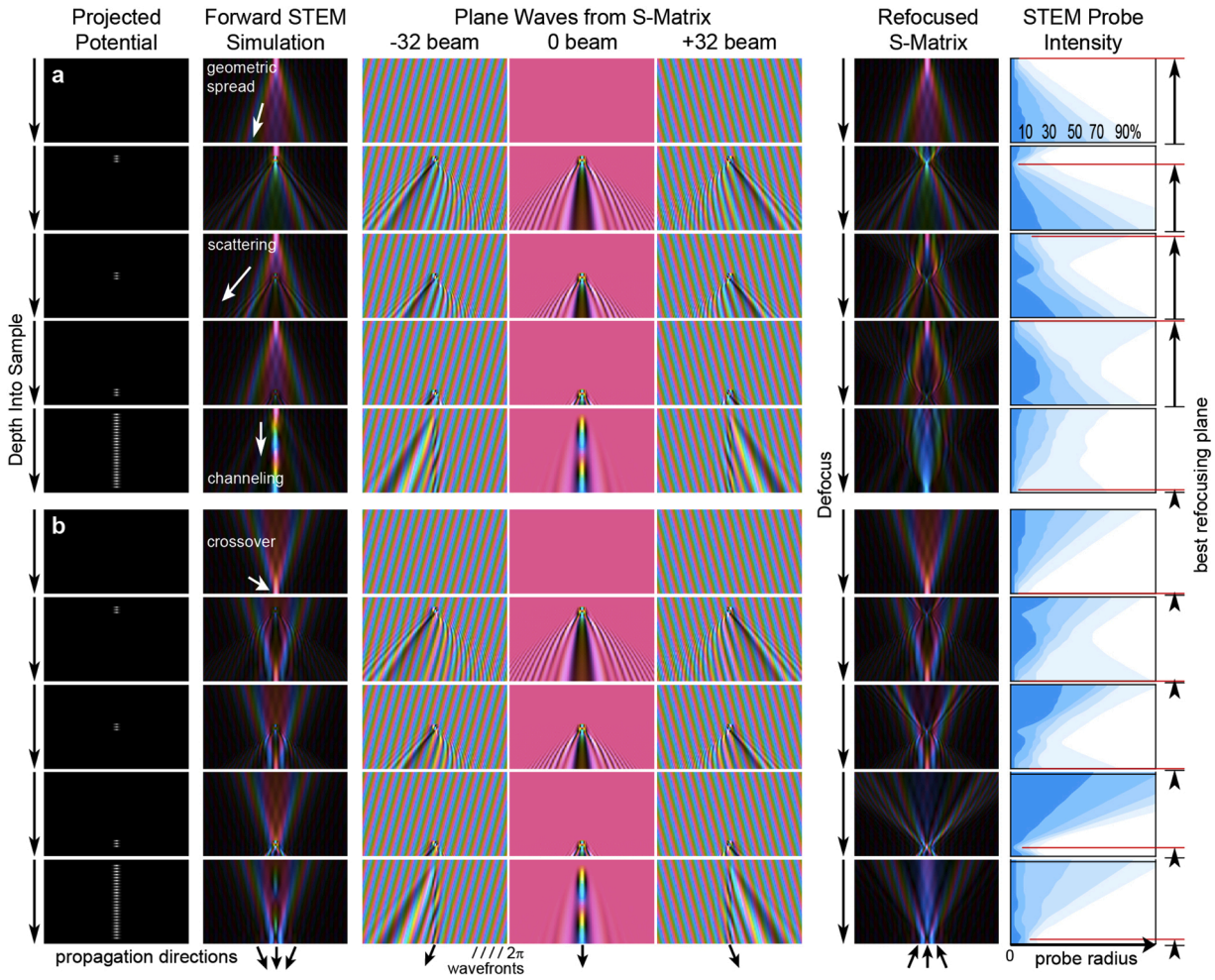

Fig. 5. Simulations demonstrating refocusing of the $\mathcal{S}$-matrix. (a) STEM probe focused at the entrance surface (top) of the sample, and (b) probe focused at the exit surface (bottom). The row cases considered in each row are (1) an empty cell, (2) small sample near top of cell, (3) small sample in middle of cell, (4) small sample at bottom of cell, and (5) sample running through entire cell. After $\mathcal{S}$-matrix is propagated through the full cell, it can be refocused to any plane before intensity is calculated. STEM probe intensity column shows the radius containing different fractions of the probe as a function of defocus. Phase of all complex waves is shown using a cyclic color scale, similarly to Fig. 4. We note that these simulations are chosen with an arbitrary sample size and beam energy, and this schematic is intended to generally depict the behavior of a propagated scattering matrix undergoing refocusing.

$2\pi\widehat{C}^{\mathrm{mag}}_{m,n}/(m\lambda)$. With this basis set, it is relatively simple to describe aberrations and provide input data in the form of delimited text files. In Fig. 4, we showcase aberration phase plates at 300 kV up to 2 inverse angstroms, for spherical aberration, 3-fold astigmatism, axial coma, and an arbitrary mixture of the above with defocus ($C_{2,0}$) and 4-fold astigmatism ($C_{4,4}$).

3.6. Refocusing of the scattering matrix

An inherent limitation of the PRISM algorithm lies within the interaction of the propagated probe and the cropping box applied to the scattering matrix. As the reciprocal-space sampling of the plane-wave basis set coarsens (by increasing the interpolation factor *f*), the cropping box applied to the propagated plane-waves becomes smaller. At high interpolation factors, much of the information carried by the propagated wavefunction can become destroyed or otherwise compromised as the beam spreads beyond the edges of the cropping box. The strong interaction of the beam at high interpolation factors thus severely limits the accuracy of the PRISM method. This becomes a more prominent effect when simulating thick samples, due to the natural broadening of the converged beam as it propagates through the sample, or when simulating STEM probes with large defocus values which are already large in extent. To overcome this limitation of the PRISM method while still retaining the computational speed-up achieved with large interpolation factors, we propose scattering matrix refocusing, an algorithmic technique which can be used to boost the accuracy of PRISM simulations with significant beam spread.

The scattering matrix *S*, when calculated by the PRISM algorithm, represents a basis of propagated plane waves which are inherently in focus at the entrance surface of the sample. To reduce the severity of the converged probe interaction with the cropping box once the probe is calculated from *S*, we apply a free-space propagator to each beam within *S* to propagate the exit wave to a plane where the intensity distribution is generally known *a priori* to be more compact,

$$S_{\mathrm{refocused}} = S \otimes P \tag{21}$$

where

$$P(\Delta z) = \mathcal{F}_{\mathrm{k}\to\mathrm{r}}\{exp(-i\pi\lambda\Delta z|\mathrm{k}|^2)\} \tag{22}$$

and is applied in Fourier space by application of the convolution theorem. $S_{\mathrm{refocused}}$ can then be used to calculate the exit wavefunction without any further alterations to the image formation algorithm. Since

the propagator in Eq. (22) imparts only a phase shift to each beam, the intensity of the exit wavefunction in the diffraction pattern, where STEM intensity measurements are recorded, is unaffected.

One way to interpret the mechanism of matrix refocusing is as shifting of the optical plane at which the cropping box is applied. In the original PRISM algorithm, the cropping box is applied at the exit surface of the sample. With refocusing, the cropping box can instead be thought to be applied at the point along the optic axis where the propagated probe is most converged – therefore, the probe has minimal opportunity to interact with the cropping box and errors that may have otherwise been incurred by application of the cropping box itself are reduced.

The process is illustrated in Fig. 5 where the refocusing procedure is applied to beams focused on the entrance, Fig. 5(a), and exit surfaces, Fig. 5(b), of different samples. The electrostatic potential $V(\mathbf{r})$ of different fictitious samples is shown in the leftmost panel of the figure and includes samples with no atoms, atoms at the top surface, an atom mid-sample, an atom at the bottom surface and a single column of atoms. The simulated complex wavefunction of a STEM probe is plotted for each of the samples in the next column. For the vacuum sample the converged probe is seen to spread from its crossover point in Fig. 5(a) and condense to its crossover point in Fig. 5(b). For the cases where single atoms are introduced at the top, middle and bottom of the sample we see electron scattering to high angles emanating from the positions of these atoms. For the case of a column of atoms we see beam channeling behavior characteristic of STEM (Hovden et al., 2012) in Fig. 5(a) where the beam couples to the column at its crossover point atop the sample. This channeling behavior is diminished for the equivalent panel in Fig. 5 (b) since the beam is not brought to cross over until the exit surface of the sample. The next 3 columns in the figure show how the constituent plane waves that form the basis of the $\mathcal{S}$-matrix interact with the specimen. In simulation we can "refocus" the exit surface wave function to any arbitrary plane within the specimen by freespace propagation of the exit wave as described previously and a depth section of the exit wave propagated to different planes is plotted in the second to last column of Fig. 5 for each of the different cases. The final column plots the radially integrated intensity of each wavefunction. We aim to find the plane where the wave-function is most compact and apply the PRISM cropping box after propagating the exit wave to this plane. For all but one of the cases in Fig. 5(a) this plane is close to the entrance surface of the specimen – i.e. the crossover point of the probe – for the case of the column of atoms channeling of the beam down the column means that the exit surface of the specimen is the plane where the exit wave function is most compact. In Fig. 5 the beam is always more compact toward the exit surface of the specimen. These results suggest that the original crossover point of the incident STEM probe is generally the plane where the beam is most compact after propagation even after interaction with the sample except for the case where strong channeling of the beam by a column of atoms occurs. This principle can be used to guide selection of the optimal plane for $\mathcal{S}$-matrix refocusing and subsequent cropping.

3.7. Post-processing

A crucial aspect of bridging the interpretation gap between "perfect" simulated images to those acquired in experiment is to process the simulated image in ways that model experimental distortions and noise conditions. These corrections are becoming increasingly important given the advent of high-throughput workflows using machine learning, such as automated analysis (Zhang et al., 2020) and denoising (Vincent et al., 2021) with deep neural networks, which require large amounts training data with latent space distributions similar (or, ideally, equivalent) to that of the target application data. In this release of `Prismatic`, we have implemented a small series of post-processing routines into the `pyprismatic` package to supplement the standard simulation routine so that coherence effects, dosage effects, and aberration effects as previously described can be easily applied to simulated data.

3.8. Coherence effects

An implicit assumption in image simulation is that electrons emanate from an ideal, infinitesimal point source, whereas in reality, imaging electrons are emitted from a finite area of the surface of the electron emitter with varying energies and thus some degree of quantum partial spatial and temporal incoherence. Spatial coherence effects for modern electron microscopes, equipped with field emission gun sources such that the distribution of incident angles is relatively small, can be accounted for through integration of independently propagated wave functions by assuming spatial coherence Allen et al. (2004). The detected wave function can then be described as

$$\Psi(\mathrm{k}) = \int \Psi_0(\mathrm{k}) exp[i\chi(\mathrm{k}+\mathrm{k}_\beta)]p(\mathrm{k}_\beta)d\mathrm{k}_\beta \tag{23}$$

where k is the wave-vector nominally in the direction of propagation, $p(\mathbf{k}_\beta)$ is a probability density function describing the distribution of incident directions, and χ is the aberration function given by Eq. (20) which models the aberrations of the post-specimen HRTEM objective lens. Including the effects of spatial coherence in HRTEM simulation, then, can be easily achieved by simulating a set of tilted plane waves up to the spread of incident directions and performing incoherent averaging of their intensities once aberrations effects have been included.

For STEM simulations, we can apply spatial coherence effects by considering finite source-sizes through a convolution model. While the precise distribution describing source-size broadening effects can be quite complex (as shown when measured through holography (Verbeeck et al., 2012)), source-size effects on the detected image can be well approximated by the convolution of the final image intensity with a blurring kernel such that

$$I_{\mathrm{blurred}}(\mathrm{r}) = I(\mathrm{r}) \otimes K \tag{24}$$

where I is the image intensity and K is a blurring kernel.

`Prismatic` has implemented source-size effects for postprocessing of STEM images through convolution with standard kernels; kernel functions for Gaussian and Cauchy kernels are included, which can adequately represent the effects of source-size blurring for most uses (Verbeeck et al., 2012). Convolution is performed with unit kernel normalization such that the intensity distribution maintains its physical definition as a probability density function for detection of scattered electron. Source-size blurring by means of convolution can be applied independently and in any order with any other incoherent averaging procedure, such as the averaging over frozen phonon configurations.

Chromatic aberration (C_c) is a temporal coherence effect that occurs as a result of the non-uniform energy of imaging electrons as emitted by the electron gun. Lower energy electrons are deflected more strongly by a magnetic lens than higher energy electrons, resulting in an energy-dependent focal point of the microscope lenses. C_c becomes the dominant aberration when C_s corrective lenses are introduced and becomes more important when low energy beams are used for imaging, as shown by the C_c limited resolution

$$r_{\mathrm{chr}} = C_{\mathrm{c}}\frac{\Delta E}{E_0}\beta \tag{25}$$

where E_0 is beam energy, ΔE is energy spread, β is the angle of collection, and C_c is the chromatic aberration coefficient. Ignoring any issues in instrument power supply, the standard deviation of defocus Δz can be obtained through the following relationship

$$\Delta z = C_{\mathrm{c}}\frac{\Delta E}{E_0} \tag{26}$$

where ΔE is the energy spread in the electron gun (Williams et al., 2009). Assuming the spread of incident beam energies is small, temporal coherence effects can be analogously included as an integration over the

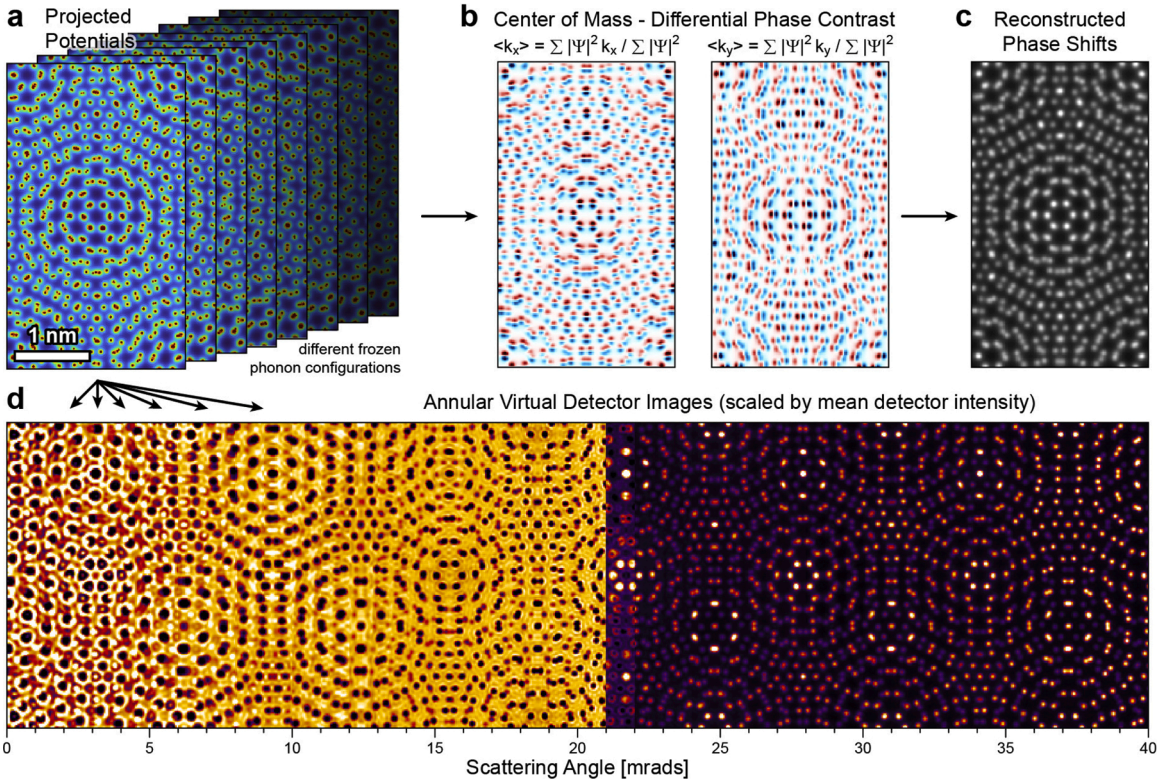

Fig. 6. A STEM imaging simulation of a WS_2 bilayer, with a twist angle of 7.34°. (a) Projected potentials of 8 frozen phonon configurations. (b) Output center-of-mass measurements, which were used as inputs for (c) the sample's reconstructed phase using the iterative method described in Savitzky et al. (2021). (d) Slices of the output virtual images from annular detectors, with the intensity of each bin normalized.

distribution of focal planes, as done for incident angles in Eq. (23). Thus, chromatic aberration effects can be accounted for in simulated results through incoherent averaging of propagated wavefunctions at a series of focal planes.

3.9. Shot noise

Modern STEM experiments are often noise limited by the maximum dose a sample can tolerate (Egerton, 2013). As a series of discrete electron scattering events, dose-limited noise profiles are well modeled by Poisson distributions. Applying Poisson noise to simulated images (which exist as evaluations of quantum-mechanical probabilities) is thus one of the most important post-processing steps for comparing simulated images and experimental images.

`Prismatic` implements Poisson noise application for HRTEM images with electron dose measured in counts per area; for STEM images, dose is applied in counts per probe. For both, intensities are scaled by the relevant measure of electron dose and then pixel counts are sampled from a Poisson distribution using the scaled intensities as independent variances. To avoid degradation of the electron distribution statistics, application of Poisson noise is performed as the final step of post-processing for any simulated images.

3.10. Unit tests

An important aspect of sustainable open-source development is to create development resources that invite outside contributions. For scientific simulation and analysis software packages, it is also critical to ensure that workflows utilizing the package produce accurate, reliable, consistent, and reproducible outcomes over the software development lifetime. In the most recent release of `Prismatic`, we have implemented a unit test suite that addresses some of these needs by testing the performance of modular sections of the code, ensuring that the new functions run accurately with respect to a set of defined behaviors. The unit test suite offers developers a simple and convenient development space to test new features and ensure that new features do not compromise the core functionality of the source code. For example, a `Prismatic` unit test testing data input and output routines might check that data are stored and read consistently for all arrays regardless of dimensionality or that the 2D vs 3D potential integration methods return physically consistent results. A new feature with a well-written unit test is much more easily adopted into `Prismatic` than untested code, and provides another route to invite community contribution to our open-source package. `Prismatic`'s test suite was implemented with the Boost unit test framework, a light-weight open-source library for integrating unit tests.[1]

4. Results and discussion

The previously described multislice and PRISM algorithms, as well as HRTEM simulation, *S*-matrix refocusing, simulation series, and arbitrary probe positions, have been implemented in the newest release of `Prismatic`, alongside utility features such as data importing and an updated GUI. Brief discussion of these implementations will follow, to serve the ongoing need of documenting open-source scientific software. Relevant case studies to the microscopy community will be shown in conjunction with each major feature that is discussed.

[1] The Boost library is an open-source, platform-independent C++ library aimed at extending the capabilities of the standard template library with minimal overhead, see https://www.boost.org

4.1. Running a STEM imaging simulation

One of the primary uses of `Prismatic` is to perform imaging simulations for STEM experiments. Fig. 6 shows one such example, simulating the interaction of a STEM probe with a bilayer of WS_2 with a twist angle of 7.34°. This simulation was performed using `pyprismatic` with these settings:

```
m                          = pyprismatic.Metadata()
m.E0                       = 200
m.probeStep                = 0.2
m.algorithm                = "p"
m.interpolationFactor      = 2
m.save3DOutput             = True
m.saveDPC_CoM              = True
m.savePotentialSlices      = True
m.probeSemiangle           = 21
m.potBound                 = 3.0
m.numFP                    = 8
```

Fig. 6a shows the projected potentials for 8 different frozen phonon configurations, using the 3D integrated atomic potentials. These arrays can be saved in the output HDF5[2] file, for further quantitative analysis.

In this simulation, we have stored the outputs of two common STEM imaging modalities using additional "save" parameters. The first output is the expectation value of the diffracted STEM probe's momentum, shown in Fig. 6b for the k_x and k_y directions. The changes in the probe's "center-of-mass" (COM) momentum $\langle \mathbf{k}_{\mathrm{CoM}}(\mathbf{r}) \rangle$ as measured in the diffraction plane,

$$\left\langle \mathrm{k}_{\mathrm{CoM}}(\mathrm{r}) \right\rangle = \frac{\int |\widehat{\mathcal{F}}_{\mathrm{r}\to\mathrm{k}}\psi(\mathrm{r})|^2 \, \mathrm{k}\, d\mathrm{k}}{\int |\widehat{\mathcal{F}}_{\mathrm{r}\to\mathrm{k}}\psi(\mathrm{r})|^2 \, d\mathrm{k}} \tag{27}$$

as it is scanned across atomic sites is clearly visible as an initial rise and then fall for each site. These signals can be directly measured in a STEM experiment, either by segmented detectors (Shibata et al., 2010) or from pixelated detectors (Ophus, 2019; Müller-Caspary et al., 2019) as in the simulation here. These measurements are usually intended for differential phase contrast (DPC) measurements. There are various ways to reconstruct the phase shift of the sample from these COM-DPC signal channels, including the iterative method described in Savitzky et al. (2021) and shown in Fig. 6c.

The second output is for monolithic annular detectors, which are commonly used for annular bright field or dark field imaging. For maximum flexibility, `Prismatic` integrates the diffracted probe intensity using virtual detectors shaped in concentric rings. These rings are finely sampled (the default bin width is 1 mrad), so that the user can generate many different annular detector configurations from a single simulation. For example, in this simulation a bright field image can be generated by summing the intensity outputs from 0 to 21 mrads. The contrast of the different bins are shown as vertical slices in Fig. 6d.

4.2. Running a 4D-STEM simulation

Fig. 7 shows 4D-STEM outputs from a simulation of the same WS_2 sample shown in Fig. 6. The projected potentials and probe positions are shown in Fig. 7a and b, while the diffracted probe intensities are shown in Fig. 7c. These probe positions span 3 atomic sites, and the DPC signal at these sites manifests as a shift of the average moment towards these sites. Additionally, when some portion of the STEM probe overlaps with these sites, a significant number of electrons are scattered outside of the initial probe's angular range. The simulation settings of this example are

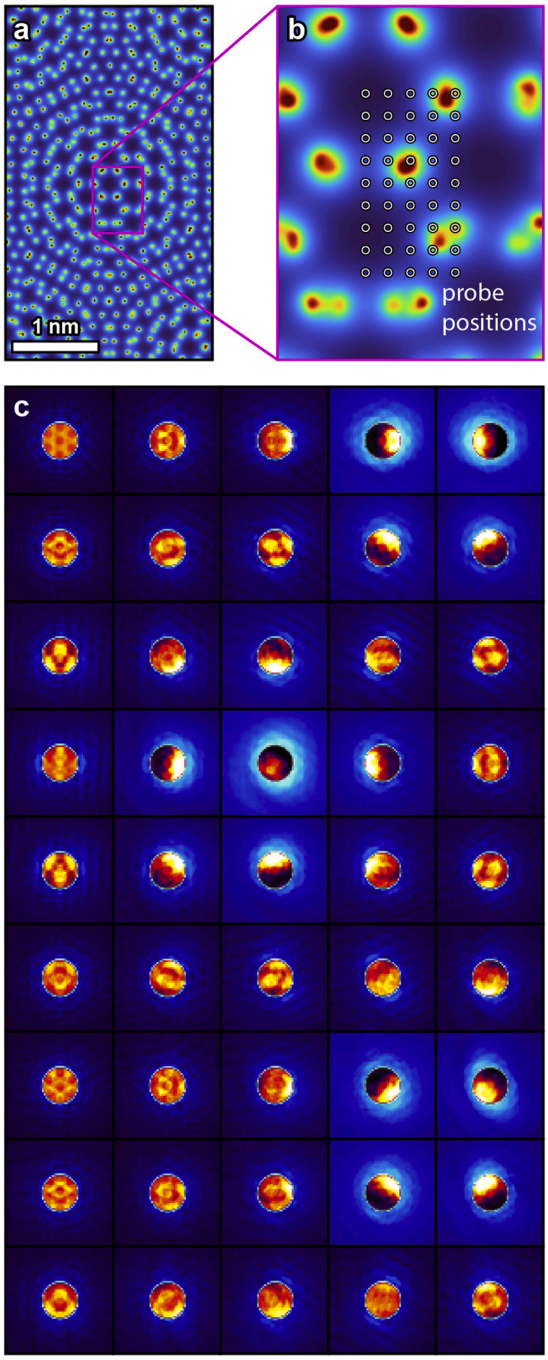

Fig. 7. A 4D-STEM simulation of a WS_2 bilayer, with a twist angle of 7.34°. (a) Projected potential, and (b) enlarged projected potential with probe positions overlaid. (c) Diffraction space images for the probe positions given in (b). Note that 2 separate intensity ranges and color maps were used inside and outside of the initial STEM probe angular range.

nearly identical to the previous simulation, except for these changes:

```
m.probeStep                = 0.5
m.save4DOutput             = True
m.scanWindowX              = (0.0, 0.1)
m.scanWindowY              = (0.0, 0.1)
```

Note that in Fig. 7a, the potentials have been shifted by half of the total cell dimensions in x and y, in order to place the probe positions in the center of the figure. No discontinuity is visible at the cell boundaries, due to the periodicity of the input cell and the simulation.

[2] The data storage format known as "hierarchical data format" version 5 (HDF5) is aimed at storing large amounts of data for which libraries and APIs are freely available see, https://www.hdfgroup.org/solutions/hdf5/.

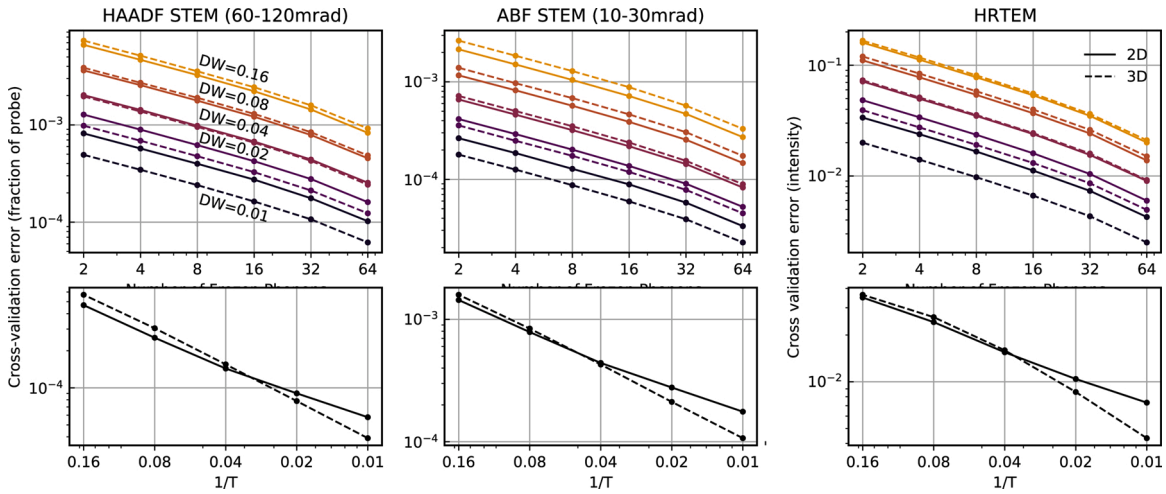

Fig. 8. Thermal convergence series for simulations of twisted bilayer WS_2. Results shown for HAADF-STEM (left), ABF-STEM (middle), and white-atom HRTEM (right). Convergence error is measured through cross-validation of sets of frozen phonon configurations (see main text for full description of error measurement). Top plots in each column represent five different temperature simulations with convergence error measured for sets of 2 through 64 frozen phonon configurations; labels indicate input Debye–Waller factor for RMS displacement of atomic positions. Bottom plots in each column show the trend in convergence error as a function of inverse temperature for simulations with 64 frozen phonon configurations. Colors in the top row indicate relative temperature. Solid lines indicate 2D potential integration and dashed lines indicate 3D potential integration with subpixel shifting.

4.3. Running an HRTEM imaging simulation

Performing HRTEM simulations in `pyprismatic` is similarly simple, with notation as follows for a plane wave simulation with complex valued output (before integration into intensity):

```
        m.algorithm                = "t"
m.saveComplexOutputWave            = True
```

We include example Jupyter notebooks for other imaging scenarios in the `Prismatic` repository.

4.4. Comparative thermal convergence of potential parameterization methods

The previous version of `Prismatic` used 2D lookup tables for the projected atomic potentials. In this release, we have implemented 3D lookup tables for the atomic potentials with subpixel shifting of the atomic sites as previously described above. The 3D potential integration scheme with subpixel shifting can improve the accuracy of a scattering simulation by offering a more realistic representation of a sample in terms of its projected potential. This is accomplished through more accurate accounting of atomic positions along the beam direction via 3D integration and perpendicular to the beam direction through subpixel shifting. Calculation of the projected potential is thus much less sensitive to the input simulation parameters such as slice thickness and projected potential resolution. In a 2D integration scheme, incorrect setting of these parameters can introduce artifacts; for example, atoms can jump unstably across slices and from pixel to pixel in the transverse direction under thermal perturbations. Here, we examine further how the two projected potential integration techniques compare under frozen phonon convergence tests. Since these schemes generate fundamentally different projected potentials at a given level of resolution, we can expect them to display qualitatively different convergence behavior over a range of temperature conditions.

To investigate the comparative convergence behavior of the projected potential integration schemes with respect to number of frozen phonons, we simulated both STEM and HRTEM images of twisted bilayer WS_2 at a 7.34° moiré angle. The convergence of scattering simulations with respect to the number of frozen phonon configurations for two-dimensional materials requires more frozen phonons than for a thicker sample because fewer unique atomic configurations can be sampled in the beam direction for any given frozen phonon configuration. Some results studying the precise thermal convergence of scattering simulations include those by Aarholt et al. (2020). The moiré cells were simulated at 80 kV with a real space potential input resolution of 0.075 Å, a 2 Å slice thickness, and a sampling factor of 40 for 3D potential integration. 128 unique frozen phonon configurations were generated for each simulation, with increasing Debye–Waller factors from 0.01 to 0.16 in multiplicative steps of 2 representing five distinct temperatures for the sample; results for each frozen phonon were saved independently. STEM simulations utilized the PRISM algorithm at an interpolation factor of 2 and a probe step size of 25 pm over a 16× reduced window of the input cell.

Convergence results are shown in Fig. 8. Convergence was measured at each of these five represented temperatures for HAADF STEM with detector angles between 60 and 120 mrad; for ABF STEM with detector angles between 10 and 30 mrad; and for HRTEM with a single untilted plane wave. To measure convergence, we used a k-fold cross-validation based scheme. For each number N of frozen phonons averaged, we generate 64 unique subsets of N configurations from the set of 128 total configurations. We then form the incoherently averaged image for each subset, measure the pixel-wise standard deviation of the intensities between the different subsets, and finally measure the mean over the field-of-view of the standard deviations. At no point are results from the differing projected potential integration schemes directly compared.

Here, we note that the convergence rate with respect to frozen phonons is largely similar across both simulation modes and temperatures. Overall cross-validation errors for both schemes drop as temperature drops. This is expected, as there is less variance in the overall atomic positions of the sample. At higher temperatures, the 3D potential with subpixel shifting scheme has comparatively higher cross-validation error, which drops below the 2D potential scheme without subpixel shifting as the temperature decreases and progressively drops faster. Crossover temperatures for cross-validation error between the two schemes occur at different points for HAADF STEM as compared to ABF STEM and HRTEM. The crossover point ultimately results from the difference in convergence behavior between the two schemes and can be understood through a sampling argument – it is likely primarily a result of the subpixel shifting. Since the 2D potential scheme must place atoms on top of discrete pixels, it is essentially sampling a small finite set of configurations for each atom, while the 3D potential with subpixel shifting samples the true continuous distribution. At high temperatures,

it is easy for the 2D potential scheme to saturate a statistically significant sampling of this finite set, while at low temperatures, it becomes difficult to perturb the atom far enough to generate different projected potential slices. In contrast, the 3D potential with subpixel shifting scheme can appropriately sample its distribution of frozen phonon configurations at all temperatures, leading to improved convergence behavior at low temperatures and slightly worse convergence at high temperatures. Again, we note that the representation of the sample given by the 3D potential with subpixel shifting integration scheme is fundamentally more physically realistic and consistent against simulation parameters than 2D potentials without subpixel shifting. While the new scheme is more computationally expensive, the importance of this difference in physicality should guide the usage of the technique in simulations, especially since, for large scale simulations, the computation of the projected potential is still an overall negligible cost as compared to the computation of wavefunction propagation.

4.5. Comparison of soft and hard probe apertures in STEM diffraction

The differences in aliasing behavior between soft and hard STEM probe apertures can be hard to predict for an actual simulation. It is important to remember that aliasing effects may not always arise as ringing artifacts in simulations. In Fig. 9, we demonstrate the differences in simulation behavior between soft and hard aperture probes for STEM diffraction of a $SrTiO_3$ crystal at 80 kV with a 4 mrad probe, for both multislice and PRISM simulations. The PRISM simulations were run with an interpolation factor of 2. All simulations were run with 3D potentials, a 0.1 Å pixel size, and 64 frozen phonons. For the multislice simulations, there is no discernible difference in the intensity or contrast of the diffracted disks between the soft apertures. For the PRISM simulations, however, there is a significant difference in the contrast (and apparent shape) of the disks, and it is seen that the soft aperture PRISM simulation much more accurately matches that of the multislice simulation. While not every use case or simulation may show such drastic differences, the soft aperture probe will overall improve the accuracy of any simulation and is more likely to be a crucial component in improving the quality of inexpensive simulations, with coarser samplings and smaller input simulation cells.

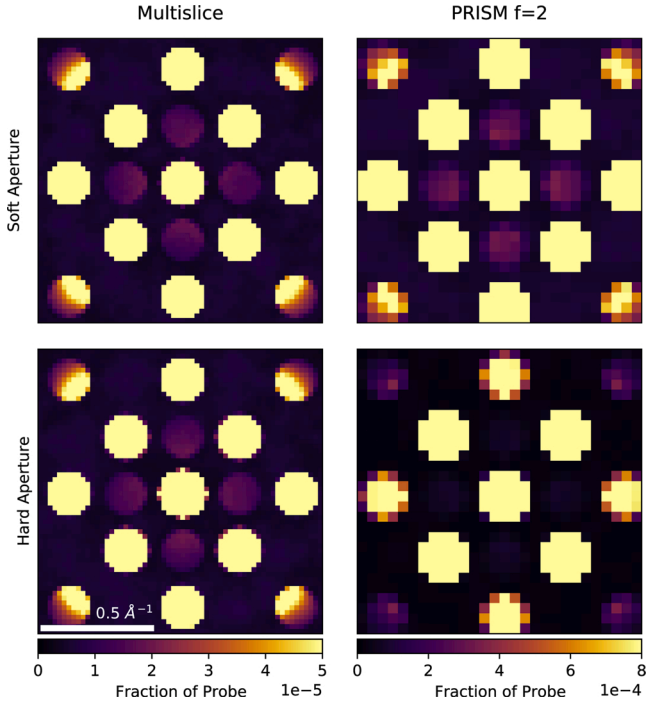

Fig. 9. STEM diffraction simulation of $SrTiO_3$. Comparative diffraction simulations for STEM diffraction of $SrTiO_3$ at 80 kV and with a 4 mrad probe semiangle for multislice and PRISM simulations with both soft and hard probe apertures. Simulation of a $12 \times 12 \times 16$ unit cell block of $SrTiO_3$ with 64 frozen phonons; input probe is placed above the center of a Sr site. Color scale is set to have equivalent contrast between multislice and PRISM simulations.

4.6. Low-dose STEM with source size effects

The effect of a finite source-size upon the simulated STEM images of twisted bilayer WS_2 at 100 kV are shown in Fig. 10, panels (a) and (b) for the as-simulated HAADF image and the HAADF image convolved with a Gaussian kernel with a FWHM of 80 pm, respectively. The effect of Poisson noise is demonstrated in Fig. 10 panel (c) for a dose rate of 5000 counts per probe.

4.7. Limited coherence effects in STEM simulations

In `Prismatic`, it is now easy to account for coherence effects caused by chromatic aberration by performing defocus series simulations. As a case study, we present convergence results for chromatic aberration effects against the number of defocus planes simulated. STEM simulations of twisted bilayer WS_2 at a 7.34° moiré angle were performed at 20 kV and 100 kV over a defocus range of ±150 Å and ±30 Å, respectively, with 65 focal planes each, a potential resolution 0.1 Å and a probe

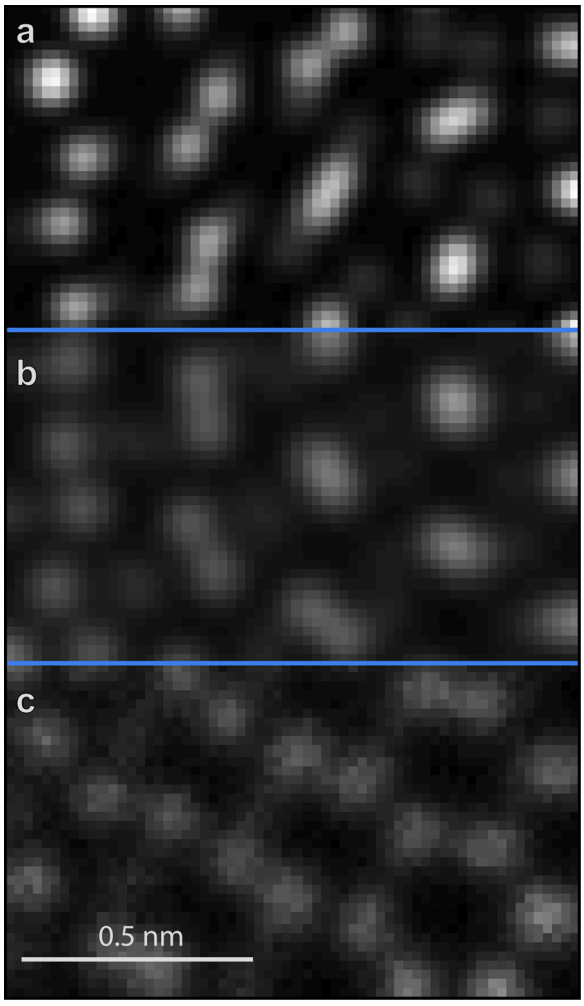

Fig. 10. HAADF-STEM image of twisted bilayer WS_2. (a) As-simulated, (b) convolved with Gaussian source-size of 80 pm FWHM, and (c) convolved with Gaussian source-size of 80 pm FWHM and with applied Poisson noise of 5000 counts per probe.

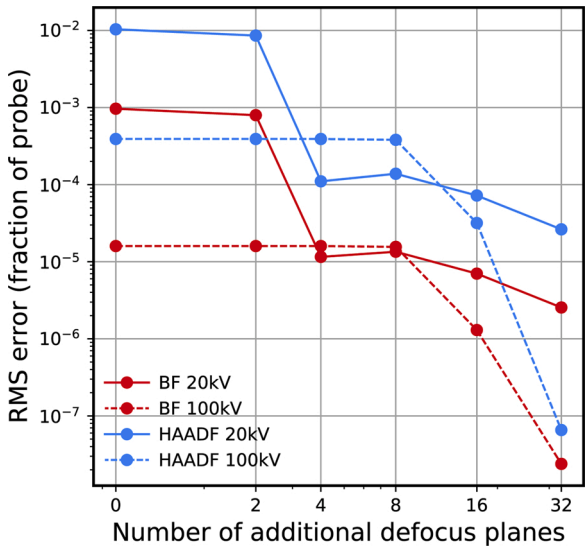

Fig. 11. Convergence series of chromatically-aberrated STEM simulations. Results for BF (red) and HAADF (blue) STEM for twisted bilayer WS_2 at 20 kV (solid) and 100 kV (dashed) with defocus spreads of 50 Å and 10 Å, respectively. Error is measured as the root-mean square error of total probe intensity against the fully averaged STEM image.

step size of 20 pm. We note for clarity that each defocus series was performed with a single execution of the simulation code, and that `Prismatic` provides new output formats that allow for easy data access for such simulation series.

The PRISM method was used with an interpolation factor of 2; we note that PRISM is a doubly advantageous technique for defocus series simulations even at an interpolation factor of 1 as the scattering matrix can be reused for each defocus value, whereas in multislice, each probe for each defocus must be simulated independently. For convergence, we measure the pixelwise root-mean-square error of a series of images averaged against differing numbers of defocus planes. In computing the defocus spread Δz, we used a fixed energy spread for both operating voltages; the defocus spreads we used were 50 Å and 10 Å for beam energies of 20 kV and 100 kV, respectively. Results for these two simulations are shown in Fig. 11. As expected, the fraction of probe error at 100 kV in both bright field and HAADF detectors is very low in all cases; at 20 kV, where the energy spread is more substantial, the error is more significant when including less than four additional defocus planes (five planes in total).

4.8. Limited coherence effects in HRTEM simulations

With the reuse of the *S*-matrix infrastructure, in `Prismatic`, we have easy access to tilt-series HRTEM simulations. Tilt series can be used to model coherence effects, for example, or experimental procedures like precession electron diffraction. Here, we will showcase simulation results taking advantage of this infrastructure to model spatial coherence effects that can arise in HRTEM experiments. We continue with WS_2 as a model material. This time, to ease the image interpretation, we simulate a monolayer WS_2 cell that is approximately 317 Å by 183 Å in size. Simulations were performed at 300 kV with an input real-space resolution of 0.075 Å in each direction; eight total simulations were run, each with four values of defocus – 2.6 nm, 9.8 nm, 31.4 nm, and 56.9 nm relative to the middle of the monolayer – to represent different contrast mechanisms and over two ranges of output tilts, ±3 mrad and ±15 mrad. For each set of simulated tilts, we perform incoherent averaging of the plane-waves with Gaussian weights up to $\pm 3\sigma$ to emulate spatial coherence effects, where σ is the standard deviation of the beam tilt. We similarly include temporal coherence effects by incoherently averaging each tilt series over a range focal planes with Gaussian weights for a focal spread with 10 Å standard deviation for each simulation. Results are shown in Fig. 12 for coherence levels σ of 0.0, 0.3, 1.0, and the unrealistically poor 5.0 mrad. As shown, emulating spatial coherence effects in this manner captures well the loss of contrast at high defocus. For small σ a large input cell is needed to achieve proper sampling of tilts as the resolution in Fourier space is inversely proportional to the sample size. Therefore, modeling these effects is more computationally intensive, particularly with regards to memory, than a typical HRTEM simulation; on a workstation with a 16 core Intel Xeon Gold 6130 processor, 250 GB system RAM and a Nvidia Quadro P5000 GPU (16 GB RAM), these simulations took approximately 1 min to perform for each frozen phonon, as compared to the sub-10 s simulation time for single plane-wave imaging.

4.9. Matrix refocusing of STEM simulations with large defocus

Focal series experiments are common in studies that involve 3D reconstruction, as they provide varying sets of information with respect to the sample phase. In order to validate these methods, such as through-focal tomography (Hovden et al., 2014), we often need to simulate large samples over wide-ranging defocus values. Matrix refocusing gives us an opportunity to utilize the computational advantages of the PRISM algorithm to model such large systems under extreme defocus conditions without incurring significant error that otherwise arises in the PRISM algorithm at large defocus. To demonstrate the utility of *S*-matrix refocusing, we present three CBED diffraction simulations of a 5 nm diameter Au nanoparticle in vacuum, tilted to an arbitrary off-zone axis. We compare the multislice algorithm, the PRISM algorithm with an interpolation factor of 2, and the PRISM algorithm with the same interpolation and with refocusing. The simulation was performed at 200 kV with a semi-convergence angle of 21 mrad and a real-space atomic potential resolution of 0.1 Å.

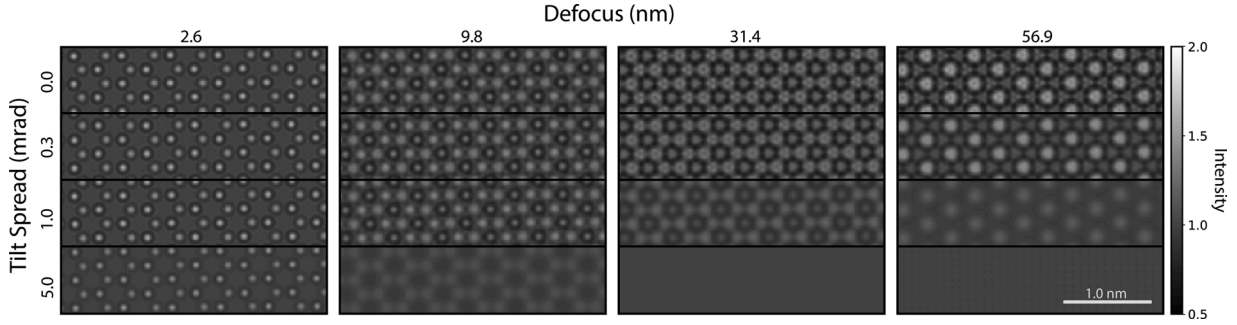

Fig. 12. Simulated HRTEM images of monolayer WS_2 at 300 kV with limited coherence. Results shown at different contrast maxima (increasing defocus left to right) and different levels of coherence (increasing tilt spread top to bottom). Images at a given tilt spread are incoherently averaged with Gaussian weights over tilted plane waves $\pm 3\sigma$ from the untilted beam. All results are similarly incoherently averaged over a focal spread of 10 Å.

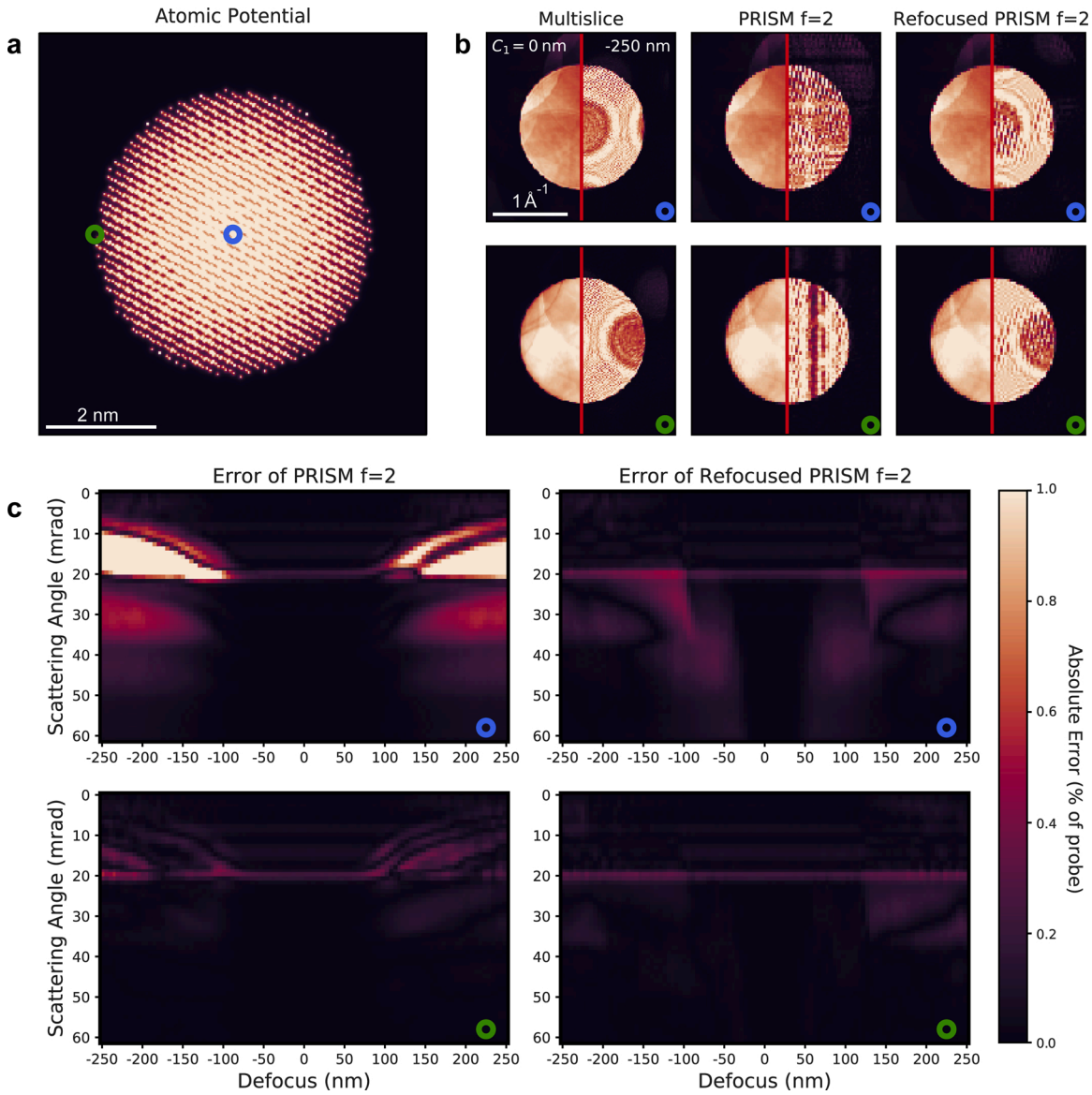

Fig. 13. Matrix refocusing results for highly defocused STEM of Au nanoparticle. Comparison of error for STEM simulations using the PRISM algorithm with and without matrix refocusing at an interpolation factor of 2, as measured against the equivalent multislice simulation. (a) Projected potential for a spherical Au nanoparticle with 5 nm diameter, tilted off-axis with center-probe and side-probe positions marked (blue and green, respectively). (b) CBED patterns for multislice (left), PRISM (middle), and PRISM with refocusing (right); panels are split between in-focus (left side) and 250 nm overfocused (right side). (c) Heatmaps of absolute error of PRISM (left) and PRISM with refocusing (right) as measured against multislice over a range of ±250 nm of defocus and over scattering angles from 0 to 60 mrad. Top panels in (b) and (c) represent probes propagated through the center of the nanoparticle, while bottom panels represent probes propagated along the side of the nanoparticle. We note the horizontal error lines visible in (c) are largely a result of coordinate artifacts that arise when comparing PRISM and multislice results; error results presently shown in (c) include slight blurring by a Gaussian kernel for purposes of visual clarity.

Results comparing the accuracy of PRISM with and without refocusing to the results of the multislice algorithm are shown in Fig. 13 for two STEM probes propagated through the center and through the edge of the nanoparticle over a defocus range of ±250 nm (measured relative to the center of the nanoparticle). Starting from the center of the nanoparticle, the PRISM algorithm without refocusing begins to accumulate significant amount of error, particularly within the center disk, as the applied defocus reaches large values (in this simulation, around ±100 nm). In contrast, PRISM with refocusing shows much more stable behavior through this defocus range within the center disk and accumulates only a small amount of error outside the beam convergence angle. At the side of the nanoparticle, both simulations show relatively consistent behavior when measuring error in binned virtual detector. There is a notable error in both methods at the edge of the center disk, which can be mostly attributed to bin assignment and precision artifacts when integrating the full pattern to the virtual detector in the simulation. When comparing against the actual 2D CBED pattern before integration onto the virtual detector, we can clearly see a great discrepancy between results using PRISM with and without refocusing. Visual comparison of the features within the center disk shows that, at large defoci, information and structure are almost completely lost without refocusing, whereas applying refocusing to the scattering matrix maintains much more of the information at high defocus values. This may be important, for example, in generating CBED images for use in applications such as machine learning, where visual similarity may be more important than integrated measures of intensity. Finally, in spite of the results presented here, we note that application of the refocusing technique is highly specific to certain imaging conditions and samples of

interest and is not a broadly applicable technique to PRISM simulations overall, and that the use of refocusing may be guided by investigating its performance on the metrics of interest for one's own application.

5. Conclusions

In this manuscript, we have presented version 2.0 of our `Prismatic` code for simulation of transmission electron microscopy experiments. This version has added various features, including 3D potential integration, HRTEM plane wave simulations, refocusing of the S-matrix for STEM simulations with large probe defocus values, more accurately sampled STEM probes, and unit tests for more reliable updates of the code. In addition we have also added several post-processing methods, including simulation of coherence limits generated by source size and energy spread effects, and shot noise calculations using Poisson random distributions of electron counts. With these additions, `Prismatic` is more useful to researchers who are performing STEM and TEM simulations.

6. Code availability

The source code for `Prismatic` is available at our Github repository. For other downloads, walkthroughs, and information, please visit prism-em.com. Simulations ran using `pyprismatic` to produce figures in the manuscript can be found in the source code repositories. Other scripts and data used can be made available upon request. For purposes of manuscript review, the most current development version of the source repository can be found at the author's development repository. A full updated software release is planned to be timed with publication of this manuscript.

Declaration of Competing Interest

The authors report no declarations of interest.

Acknowledgements

L.R.D was supported by the Toyota Research Institute and by the Department of Energy Computational Science Graduate Fellowship. H. G.B. and J.C. acknowledge additional support from the Presidential Early Career Award for Scientists and Engineers (PECASE) through the U.S. Department of Energy. P.M.P and M.C.S are supported by the Strobe STC research center, Grant No. DMR 1548924. L.J. is supported by SFI-Royal Society URF award no. URF/RI/191637. P.O.D. is supported by the TCD School of Physics Summer Undergraduate Research Experience programme (SURE), P.M.B. is supported by the AMBER Research centre award no. 17/RC-PhD/3477. C.O. is supported by the USA Department of Energy Early Career Research Award program. Work at the Molecular Foundry was supported by the Office of Science, Office of Basic Energy Sciences, of the U.S. Department of Energy under Contract No. DE-AC02-05CH11231. This material is based upon work supported by the U.S. Department of Energy, Office of Science, Office of Advanced Scientific Computing Research, Department of Energy Computational Science Graduate Fellowship under Award Number DE-SC0021110.

References

Aarholt, T., Frodason, Y.K., Prytz, Ø., 2020. Imaging defect complexes in scanning transmission electron microscopy: impact of depth, structural relaxation, and temperature investigated by simulations. Ultramicroscopy 209, 112884. https://doi.org/10.1016/j.ultramic.2019.112884. ISSN 0304-3991. https://www.sciencedirect.com/science/article/pii/S030439911930107X.

Allen, L.J., McBride, W., O'Leary, N.L., Oxley, M.P., 2004. Exit wave reconstruction at atomic resolution. Ultramicroscopy 100 (1), 91–104. https://doi.org/10.1016/j.ultramic.2004.01.012. ISSN 0304-3991. https://www.sciencedirect.com/science/article/pii/S0304399104000257.

Batson, P.E., Dellby, N., Krivanek, O.L., 2002. Sub-ångstrom resolution using aberration corrected electron optics. Nature 418 (6898), 617–620.

Brown, H.G., Ciston, J., Ophus, C., 2019. Linear-scaling algorithm for rapid computation of inelastic transitions in the presence of multiple electron scattering. Phys. Rev. Res. 1 (3), 033186.

Brown, H.G., Pelz, P., Ophus, C., Ciston, J., 2020. A python based open-source multislice simulation package for transmission electron microscopy. Microsc. Microanal.

Buseck, P., Cowley, J., Eyring, L., 1989. High-Resolution Transmission Electron Microscopy: And Associated Techniques. Oxford University Press.

Cowley, J.M., Moodie, A.F., 1957. The scattering of electrons by atoms and crystals. I. A new theoretical approach. Acta Crystallogr. 10 (10), 609–619.

Das, S., Tang, Y.L., Hong, Z., Gonçalves, M.A.P., McCarter, M.R., Klewe, C., Nguyen, K.X., Gómez-Ortiz, F., Shafer, P., Arenholz, E., et al., 2019. Observation of room-temperature polar skyrmions. Nature 568 (7752), 368–372.

Egerton, R.F., et al., 2005. Physical Principles of Electron Microscopy, vol. 56. Springer.

Egerton, R.F., 2013. Control of radiation damage in the TEM. Ultramicroscopy 127, 100–108. https://doi.org/10.1016/j.ultramic.2012.07.006. ISSN 0304-3991. https://www.sciencedirect.com/science/article/pii/S0304399112001763. Frontiers of Electron Microscopy in Materials Science.

Gass, M.H., Bangert, U., Bleloch, A.L., Wang, P., Nair, R.R., Geim, A.K., 2008. Free-standing graphene at atomic resolution. Nat. Nanotechnol. 3 (11), 676–681.

Haider, M., Uhlemann, S., Schwan, E., Rose, H., Kabius, B., Urban, K., 1998. Electron microscopy image enhanced. Nature 392 (6678), 768–769.

Hovden, R., Xin, H.L., Muller, D.A., 2012. Channeling of a subangstrom electron beam in a crystal mapped to two-dimensional molecular orbitals. Phys. Rev. B 86 (19), 195415.

Hovden, R., Ercius, P., Jiang, Y., Wang, D., Yu, Y., Abruña, H.D., Elser, V., Muller, D.A., 2014. Breaking the crowther limit: Combining depth-sectioning and tilt tomography for high-resolution, wide-field 3d reconstructions. Ultramicroscopy 140, 26–31. https://doi.org/10.1016/j.ultramic.2014.01.013. ISSN 0304-3991. https://www.sciencedirect.com/science/article/pii/S0304399114000230.

Kazuo, I., Natsu, U., 1977. A new theoretical and practical approach to the multislice method. Acta Crystallogr. Sect. A: Cryst. Phys., Diffr., Theor. Gen. Crystallogr. 33 (5), 740–749.

Kirkland, E.J., 2011. On the optimum probe in aberration corrected ADF-STEM. Ultramicroscopy 111 (11), 1523–1530.

Kirkland, E.J., 2020. Advanced Computing in Electron Microscopy, 3rd ed. Springer Nature.

Kothleitner, G., Neish, M.J., Lugg, N.R., Findlay, S.D., Grogger, W., Hofer, F., Allen, L.J., 2014. Quantitative elemental mapping at atomic resolution using X-ray spectroscopy. Phys. Rev. Lett. 112 (8), 085501.

Krivanek, O.L., Mooney, P.E., 1993. Applications of slow-scan CCD cameras in transmission electron microscopy. Ultramicroscopy 49 (1–4), 95–108.

Krivanek, O.L., 1994. Three-fold astigmatism in high-resolution transmission electron microscopy. Ultramicroscopy 55 (4), 419–433.

LeBeau, J.M., Findlay, S.D., Allen, L.J., Stemmer, S., 2008. Quantitative atomic resolution scanning transmission electron microscopy. Phys. Rev. Lett. 100 (20), 206101.

Lobato, I., Van Dyck, D., 2015. MULTEM: a new multislice program to perform accurate and fast electron diffraction and imaging simulations using graphics processing units with CUDA. Ultramicroscopy 156, 9–17.

Müller-Caspary, K., Krause, F.F., Winkler, F., Béché, A., Verbeeck, J., Van Aert, S., Rosenauer, A., 2019. Comparison of first moment stem with conventional differential phase contrast and the dependence on electron dose. Ultramicroscopy 203, 95–104. https://doi.org/10.1016/j.ultramic.2018.12.018. ISSN 0304-3991. https://www.sciencedirect.com/science/article/pii/S0304399118302730. 75th Birthday of Christian Colliex, 85th Birthday of Archie Howie, and 75th Birthday of Hannes Lichte /PICO 2019 – Fifth Conference on Frontiers of Aberration Corrected Electron Microscopy.

MacLaren, I., Macgregor, T.A., Allen, C.S., Kirkland, A.I., 2020. Detectors-the ongoing revolution in scanning transmission electron microscopy and why this important to material characterization. APL Mater. 8 (11), 110901.

Madsen, J., Susi, T., 2021. The abTEM code: transmission electron microscopy from first principles. Open Res. Europe 1, 24.

Ophus, C., Ciston, J., Pierce, J., Harvey, T.R., Chess, J., McMorran, B.J., Czarnik, C., Rose, H.H., Ercius, P., 2016a. Efficient linear phase contrast in scanning transmission electron microscopy with matched illumination and detector interferometry. Nat. Commun. 7.

Ophus, C., Rasool, H.I., Linck, M., Zettl, A., Ciston, J., 2016b. Automatic software correction of residual aberrations in reconstructed HRTEM exit waves of crystalline samples. Adv. Struct. Chem. Imag. 2 (1), 15. ISSN 2198-0926. doi:10.1186/s40679-016-0030-1. URL https://ascimaging.springeropen.com/articles/10.1186/s40679-016-0030-1.

Ophus, C., 2017. A fast image simulation algorithm for scanning transmission electron microscopy. Adv. Struct. Chem. Imaging 3 (1), 13.

Ophus, C., 2019. Four-dimensional scanning transmission electron microscopy (4D-STEM): from scanning nanodiffraction to ptychography and beyond. Microsc. Microanal. 25 (3), 563–582.

Pelz, P.M., Rakowski, A., Rangel DaCosta, L., Savitzky, B.H., Scott, M.C., Ophus, C., 2021. A fast algorithm for scanning transmission electron microscopy (STEM) imaging and 4D-STEM diffraction simulations. Micrcosc. Microanal. 27, 835–848.

Pennycook, S.J., Nellist, P.D., 2011. Scanning Transmission Electron Microscopy: Imaging and Analysis. Springer Science & Business Media.

Pryor, A., Ophus, C., Miao, J., 2017. A streaming multi-GPU implementation of image simulation algorithms for scanning transmission electron microscopy. Adv. Struct. Chem. Imaging 3 (1), 15.

Robertson, A.W., Warner, J.H., 2013. Atomic resolution imaging of graphene by transmission electron microscopy. Nanoscale 5, 4079–4093. https://doi.org/10.1039/C3NR00934C.

Savitzky, B.H., Zeltmann, S.E., Hughes, L.A., Brown, H.G., Zhao, S., Pelz, P.M., Pekin, T. C., Barnard, E.S., Donohue, J., Rangel DaCosta, L., et al., 2021. py4DSTEM: a software package for four-dimensional scanning transmission electron microscopy data analysis. Microsc. Microanal. 1–32. https://doi.org/10.1017/S1431927621000477.

Shibata, N., Kohno, Y., Findlay, S.D., Sawada, H., Kondo, Y., Ikuhara, Y., 2010. New area detector for atomic-resolution scanning transmission electron microscopy. J. Electron Microsc. 59 (6), 473–479.

Spurgeon, S.R., Ophus, C., Jones, L., Petford-Long, A., Kalinin, S.V., Olszta, M.J., Dunin-Borkowski, R.E., Salmon, N., Hattar, K., Yang, W.-C.D., et al., 2020. Towards data-driven next-generation transmission electron microscopy. Nat. Mater. 1–6.

Sturkey, L., 1962. The calculation of electron diffraction intensities. Proc. Phys. Soc. (1958–1967) 80 (2), 321.

Thust, A., Overwijk, M.H.F., Coene, W.M.J., Lentzen, M., 1996. Numerical correction of lens aberrations in phase-retrieval HRTEM. Ultramicroscopy 64 (1–4), 249–264.

Uhlemann, S., Haider, M., 1998. Residual wave aberrations in the first spherical aberration corrected transmission electron microscope. Ultramicroscopy 72 (3–4), 109–119.

Van Dyck, D., 1985. Advances in Electronics and Electron Physics. Academic, New York, p. 295.

Venkatraman, K., Levin, B.D.A., March, K., Rez, P., Crozier, P.A., 2019. Vibrational spectroscopy at atomic resolution with electron impact scattering. Nat. Phys. 15 (12), 1237–1241.

Verbeeck, J., Béché, A., Van den Broek, W., 2012. A holographic method to measure the source size broadening in STEM. Ultramicroscopy. ISSN 03043991. doi:10.1016/j.ultramic.2012.05.007.

Vincent, J.L., Manzorro, R., Mohan, S., Tang, B., Sheth, D.Y., Simoncelli, E.P., Matteson, D.S., Fernandez-Granda, C., Crozier, P.A., 2021. Developing and Evaluating Deep Neural Network-Based Denoising for Nanoparticle TEM Images with Ultra-Low Signal-to-Noise.

Weinberg, S., 1995. The Quantum Theory of Fields, vol. 2. Cambridge University Press.

Williams, D.B., Barry Carter, C., 2009. Transmission Electron Microscopy: A Textbook for Materials Science, vols. 1–4. ISBN 978-0-387-76500-6. http://www.loc.gov/catdir/enhancements/fy0820/96028435-d.html.

Yang, Y., Chen, C.-C., Scott, M.C., Ophus, C., Xu, R., Pryor, A., Wu, L., Sun, F., Theis, W., Zhou, J., et al., 2017. Deciphering chemical order/disorder and material properties at the single-atom level. Nature 542 (7639), 75–79.

Zhang, C., Feng, J., Rangel DaCosta, L., Voyles, P.M., 2020. Atomic resolution convergent beam electron diffraction analysis using convolutional neural networks. Ultramicroscopy 210, 112921.